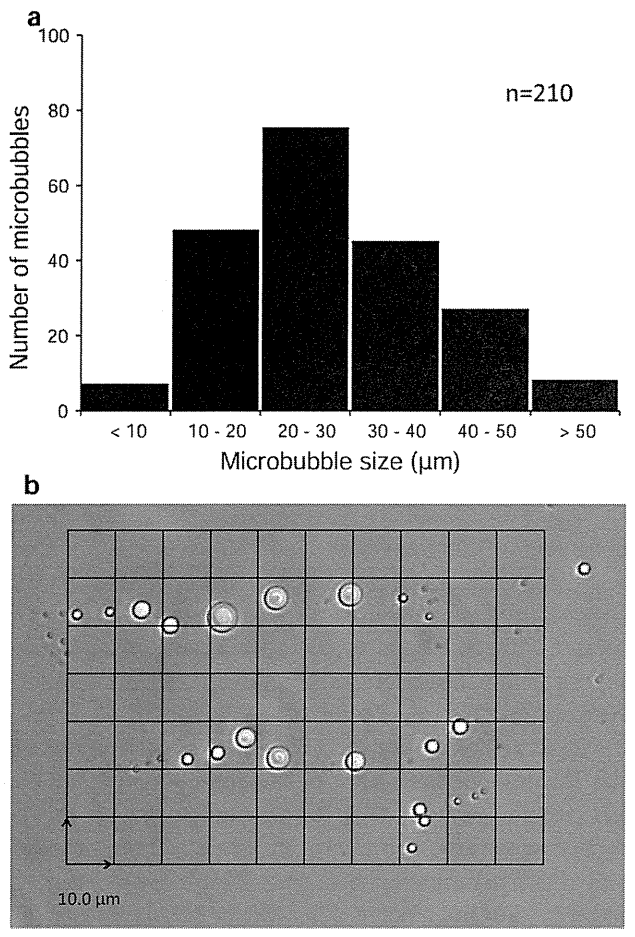

Fig. 2 Morphological analysis of generated oxygen microbubbles. a The distribution of the microbubbles generated by the micro-nanobubble aerator. b Microbubbles were inhomogeneous in size. After brief sonication, relatively large microbubbles disappeared and fine microbubbles remained. The bubbles were \6 Im in diameter and nanobubbles were also present

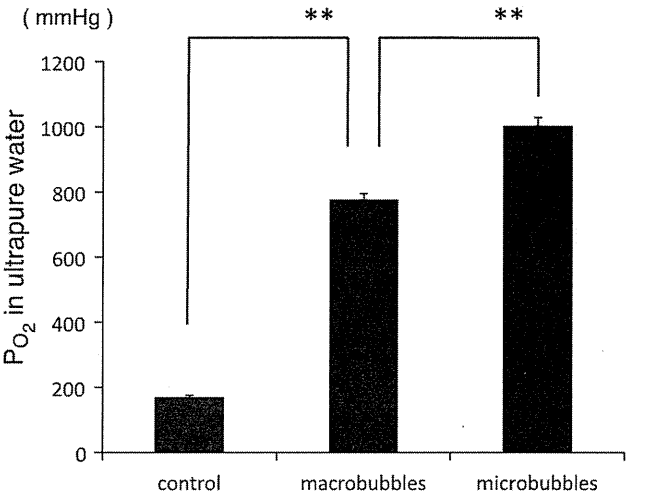

Fig. 3 Comparison of Po_2 increase in ultrapure water between oxygen macrobubbles and oxygen microbubbles. Oxygen macrobubbles were generated in ultrapure water (150 ml) by use of porous ceramic with 1 l/min oxygen gas supply for 15 min. Oxygen microbubbles were generated by use of a micro-nanobubble aerator. The Po_2 in ultrapure water was determined by blood gas analysis. Results are shown as mean ± standard error of the mean from five separate experiments, each performed in duplicate. **P \ 0.01

Effects of solvents on the Po_2 increase by microbubbles

To examine the effect of solvent on the Po_2 increase after microbubble treatment, the Po_2 in ultrapure water containing a 1, 5, or 10 % NaCl, an electrolyte, or a 5, 10, or 20 % glucose, were measured by blood gas analysis. Means were compared by ANOVA and Tukey's post-hoc test.

Figure 4a shows the effects of NaCl on Po_2 increase by use of oxygen microbubbles. On average, Po_2 values were 1,003.2 ± 25.5 mmHg in the control (P \ 0.01 vs. 5 % and 10 % NaCl solution), 985.6 ± 27.1 mmHg in 1 % NaCl solution (P \ 0.01 vs. 5 % and 10 % NaCl solution), 829.5 ± 18.6 mmHg in 5 % NaCl solution (P \ 0.01 vs. control and 1 % NaCl solution), and 745.8 ± 11.4 mmHg in 10 % NaCl solution (P \ 0.01 vs. control and 1 % NaCl solution). These results suggested that the oxygenation by microbubbles decreased with increasing concentration of the NaCl solution. Above, less than 1 % NaCl solution was enough to increase the Po_2 in the liquid by use of oxygen microbubbles compared with untreated ultrapure water.

Figure 4b shows the effects of glucose on the Po_2 increase by use of oxygen microbubbles. On average, Po_2 values were 1,003.2 ± 25.5 mmHg in the control (P \ 0.05 vs. 5 % glucose solution, P \ 0.01 vs. 10 and 20 % glucose solution), 866.3 ± 38.6 mmHg in 5 % glucose solution (P \ 0.05 vs. control), 828.3 ± 17.8 mmHg in 10 % glucose solution (P \ 0.01 vs. control), and 763.8 ± 29.8 mmHg in 20 % glucose solution (P \ 0.01 vs. control). The results suggested that oxygenation by microbubbles decreased with increasing concentration of glucose. Even 5 % glucose solution significantly inhibited the Po_2 increase by oxygen microbubbles.

Blood oxygenation by use of oxygen microbubble fluid

To examine the potency of blood oxygenation by fluid containing oxygen microbubbles, OMNSS was mixed with swine venous blood in different ratios. After mixing for 3 min at dilution ratios of 10–50 %, the Po_2 in blood samples was measured by blood gas analysis.

Figure 5a shows Po_2 values in blood diluted with 10, 20, 30, or 50 % OMNSS or NSS. Means were compared by use of unpaired t-tests. The average Po_2 in control blood (without dilution) was 64.6 ± 1.3 mmHg. Average Po_2 values were 81.9 ± 3.3 mmHg and 72.4 ± 1.5 mmHg in blood diluted with 10 % OMNSS/NSS (P \ 0.05), 89.5 ± 4.2 mmHg and 78.9 ± 2.5 mmHg in blood diluted

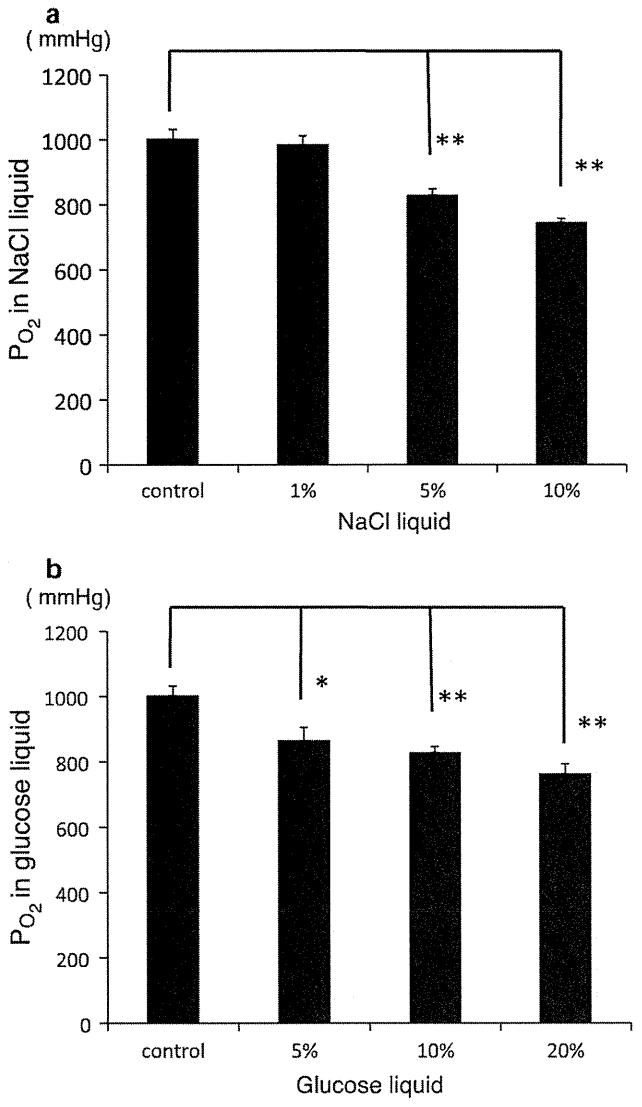

Fig. 4 Effects of solutes on the Po_2 increase in fluid resulting from use of oxygen microbubbles. a NaCl. b Glucose. Results are mean ± standard error of the mean from five separate experiments, each performed in duplicate. *P \ 0.05; **P \ 0.01

with 20 % OMNSS/NSS (P \ 0.05), 110.4 ± 8.9 mmHg and 82.1 ± 4.1 mmHg in blood diluted with 30 % OMNSS/NSS (P \ 0.05), and 166.6 ± 25.3 mmHg and 106.0 ± 13.1 mmHg in blood diluted with 50 % OMNSS/NSS (P \ 0.05), respectively. These results suggest that OMNSS results in a significantly greater Po_2 increase in blood than NSS, and the difference in Po_2 value between OMNSS and NSS becomes greater with increasing dilution ratio in the blood.

Figure 5b shows Po_2 values at 10 % dilution with NSS with and without oxygen microbubbles in blood. Means were compared by ANOVA and Tukey's post-hoc test. On average, the Po_2 values were 64.6 ± 1.4 mmHg in control venous blood (P \ 0.05 vs. 10 % OMNSS), 72.4 ± 1.5

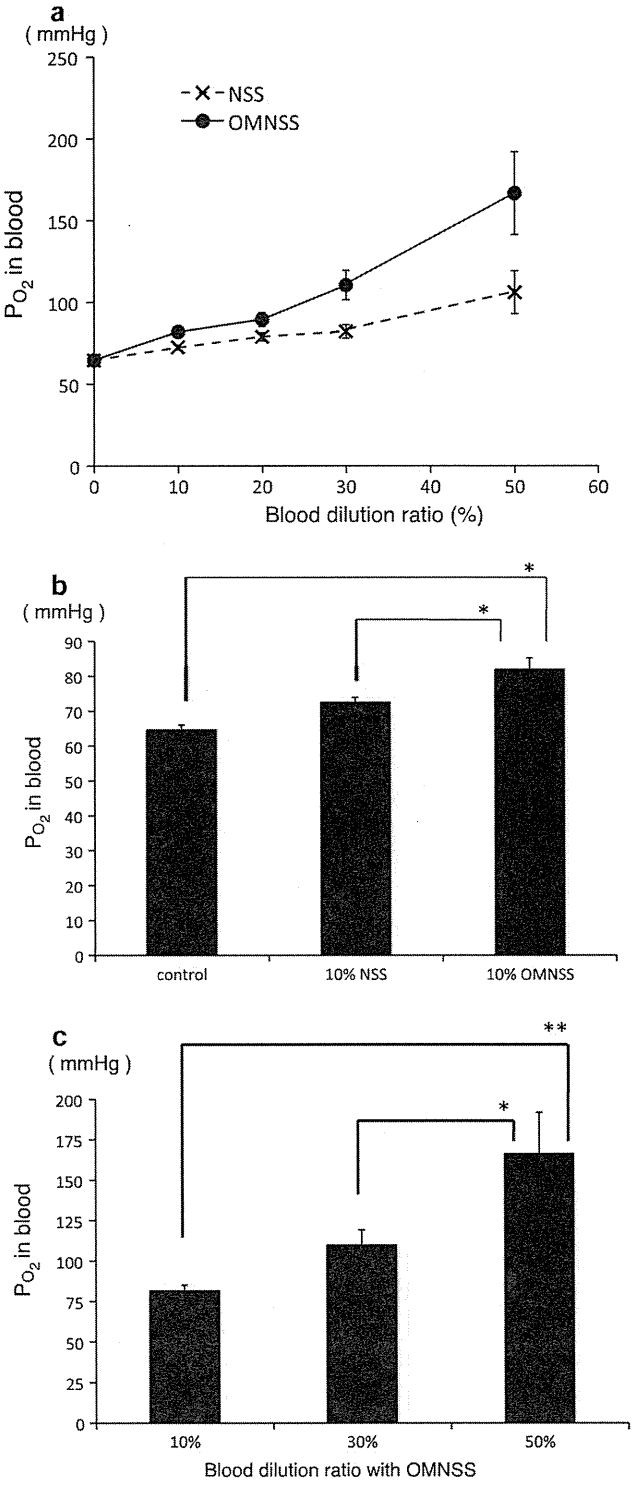

Fig. 5 Po_2 increases in blood by use of oxygen microbubble NSS (OMNSS). Swine venous blood was diluted with OMNSS at 10, 20, 30, or 50 %, and mixed gently for 3 min. The Po_2 in blood was determined by blood gas analysis. a Comparison of Po_2 increases in blood between NSS and OMNSS. b Comparison of Po_2 increases in blood at 10 % dilution with NSS or OMNSS. c Po_2 increases in blood at each dilution ratio with OMNSS. Results are shown as mean ± standard error of the mean from five separate experiments, each performed in duplicate. *P \ 0.05; **P \ 0.01

12 3

mmHg in blood diluted 10 % with NSS (P \ 0.05 vs. 10 % OMNSS), and 81.9 ± 3.3 mmHg in blood diluted 10 % with OMNSS (P \ 0.05 vs. control and 10 % diluted blood with NSS). The results suggested that OMNSS significantly improved the Po_2 in hypoxic blood.

Figure 5c shows Po_2 values in blood diluted with 10, 30, or 50 % OMNSS. Means were compared by ANOVA and Tukey's post-hoc test. The average Po_2 values were 81.9 ± 3.3 mmHg in blood diluted with 10 % OMNSS (P \ 0.01 vs. 50 %), 110.4 ± 8.9 mmHg in blood diluted with 30 % OMNSS (P \ 0.05 vs. 50 %), and 166.6 ± 25.3 mmHg in blood diluted with 50 % OMNSS (P \ 0.01 vs. 10 %, P \ 0.05 vs. 30 %). These results suggested that Po_2 in hypoxic blood was significantly increased by increasing the mixing volume of OMNSS. In addition, blood diluted with 50 % OMNSS was significantly more oxygenated than 10 % diluted blood (P \ 0.05).

Discussion

Microbubbles are gas bubbles \50 Im diameter in liquids; they have a variety of unique properties (Kurup and Naik 2010; Qin et al. 2009). In particular, their efficient and high oxygen gas solubility is beneficial for oxygenation of hypoxic tissues (Bitterman 2009; Abdelsalam and Cheifetz 2010; Raoof et al. 2010; Guo and DiPietro 2010).

In our experiments, most of the oxygen microbubbles generated after application of brief sonication were \10 Im in diameter (Fig. 2b), and were categorized as fine microbubbles (Takahashi et al. 2003, 2005, 2007). These fine microbubbles were thought to be captured as the result of the gradual shrinking of microbubbles that finally collapse. Fine oxygen microbubbles are expected to have a variety of useful properties in medicine (Barbosa et al. 2009; Betit 2009; Kulikovsky et al. 2009). Microbubbles \10 Im in diameter are thought to be clinically safe; the filter pore sizes for cardiopulmonary bypass machines are usually in the range 28–40 Im, and oxygen microbubbles 10 Im in diameter are therefore negligibly small (Barak and Katz 2005).

The most beneficial property of microbubbles is the highly efficient gas solubility, which is expressed as Po_2 increases in liquids including blood. The Po_2 values in water containing oxygen microbubbles were significantly higher than the theoretical Po_2 value (760 mmHg). According to the Young–Laplace equation, the shrinking oxygen microbubble increases the inertial pressure and oxygen gas dissolves to a much greater extent water by Henry's law. The smaller the bubble size, the higher the Po_2 value in water. In our experiments, Po_2 values in water were approximately 30 % greater than full oxygen saturation (Fig. 3). Nanobubbles must increase the Po_2 value in water to a much greater extent than microbubbles.

Next, we examined how solutes in the fluid, for example NaCl and glucose, which are commonly used in daily clinical practice, affect the increase in Po_2 by microbubbles. NaCl and glucose both inhibited the Po_2 increase by microbubbles, in accordance with their concentration (Fig. 4a). As oxygen gas has low polarity and tends to dissolve in low-polarity liquids, our results indicating that Po_2 in water was reduced by NaCl or glucose, which are polar in solution, are credible. However, NSS used in daily clinical practice is of very low concentration (only 0.9 %) and had little effect on the Po_2 values compared with the control. Therefore, NSS containing microbubbles can be a clinically useful fluid for tissue oxygenation. The Po_2 values in 5 % glucose solution were significantly (* 15 %) reduced compared with the control. Twenty percent glucose solution, which is used in intravenous hyperalimentation, had almost the same Po_2 as the theoretical maximum Po_2 value in water (Fig. 4b). Thus, fluids containing glucose are not suitable for tissue oxygenation using this method.

OMNSS increased the Po_2 values in blood in accordance with the mixing volume (ratio) (Fig. 5a). At 10 % dilution in blood, OMNSS resulted in significantly higher Po_2 than NSS (Fig. 5b). The oxygen volume in blood is expressed as follows (Scholz et al. 2010):

Total Co_2 • •a • Po_2 • b • Hb • Sat• • V

where a is the solubility coefficient of oxygen in blood (0.003 ml/l mmHg), b is the oxygen-carrying capacity of hemoglobin (1.34 ml/gHb), Hb is the concentration of hemoglobin in blood (15 g/dl), V is blood volume (5 l), and Sat is the saturation of hemoglobin.

In addition, Sat in blood under conditions of pH 7.4 at 37 •C is expressed as follows (Dash and Bassingthwaighte 2010):

$$Sat \bullet \ Ko_2 \bullet Po_2^n = \bullet 1 \bullet \ Ko_2 \bullet Po_2^n \bullet \ \bullet Po_2 = P_{50} \bullet^n \bullet 1 \bullet \ \bullet Po_2 = P_{50} \bullet^n \bullet$$

where Ko_2 is the Hill coefficient and n is the Hill exponent (n = 2.7). They are related by $Ko_2 = (P_{50})^{-n}$ where P_{50} is the level of Po_2 at which Hb is 50 % saturated by O_2 (P_{50} = 26.6 mmHg) (Goutelle et al. 2008).

In this study, the mean Po_2 of the control blood (64.6 mmHg) was improved from 81.6 to 166.6 mmHg by dilution with OMNSS. Given these data at 37 •C, the saturation value of hemoglobin was calculated to be 91.3 % at Po_2 = 64.6 mmHg, 95.2 % at Po_2 = 81.6 mmHg, and 99.3 % at Po_2 = 166.6 mmHg. The total Co_2 was calculated as 927 ml for control blood, 970.8 ml for blood diluted with 10 % OMNSS, and 1004.3 for blood diluted with 50 % OMNSS. The value of total Co_2 for blood diluted with 10 % OMNSS was 43.8 ml higher than that of the control blood; this oxygen excess corresponds to

87.6 % of the oxygen consumption of the brain per minute in adults. In addition, the value of total Co_2 in blood diluted with 50 % OMNSS was 121 ml higher than that of the control blood; this oxygen excess corresponds to 48.4 % of the oxygen consumption of the whole body per minute in adults. Therefore, the oxygen microbubble fluid described here can be locally injected into hypoxic tissues but is not sufficient for general infusion. For general infusion, it will be necessary to achieve an approximately tenfold higher density of oxygen microbubbles. This will require more innovative methods for production of finer microbubbles (nanobubbles) or shell reagents for bubbles.

In summary, finer micro-nanobubbles can be used to achieve oxygen supersaturation in fluids, and may be small and safe enough for infusion into blood vessels. Although increases in Po_2 in fluids by use of oxygen microbubbles were inhibited by polar solvents, NSS had little effect. Thus, NSS will be suitable for production of oxygen-rich fluid. In addition, OMNSS effectively improved hypoxic conditions in blood. Use of oxygen micro/nanobubble fluids is an effective novel method for oxygenation of hypoxic tissues caused by ischemia and general hypoxia, for infection control caused by anaerobic bacteria, and for anticancer treatment. However, it has been suggested that microbubbles also cause tissue damage and that oxygen itself can be toxic (Barak and Katz 2005; Dennery 2010; Wang et al. 2010; Allen et al. 2009). Further studies of fine micro/nanobubbles are required to increase the Po_2 under hypoxic conditions and to assess the effects on tissues and the whole body.

Acknowledgments This study was supported by Grants-in-Aid for Scientific Research (C) from the Japan Society for the Promotion of Science (JSPS; no. 21500402).

References

Abdelsalam M, Cheifetz IM (2010) Goal-directed therapy for severely hypoxic patients with acute respiratory distress syndrome: permissive hypoxemia. Respir Care 55(11):1483–1490

Allen BW, Demchenko IT, Piantadosi CA (2009) Two faces of nitric oxide: implications for cellular mechanisms of oxygen toxicity. J Appl Physiol 106(2):662–667

Badea R, Seicean A, Diaconu B, Stan-Iuga R, Sparchez Z, Tantau M, Socaciu M (2009) Contrast-enhanced ultrasound of the pancreas: a method beyond its potential or a new diagnostic standard? J Gastrointestin Liver Dis 18(2):237–242

Barak M, Katz Y (2005) Microbubbles: pathophysiology and clinical implications. Chest 128(4):2918–2932

Barbosa FT, Juca MJ, Castro AA, Duarte JL, Barbosa LT (2009) Artificial oxygen carriers as a possible alternative to red cells in clinical practice. Sao Paulo Med J 127(2):97–100

Betit P (2009) Extracorporeal membrane oxygenation: Quo Vadis? Respir Care 54(7):948–957

Bitterman H (2009) Bench-to-bedside review: oxygen as a drug. Crit Care 13(1):205

Cavalli R, Bisazza A, Giustetto P, Civra A, Lembo D, Trotta G, Guiot C, Trotta M (2009) Preparation and characterization of dextran nanobubbles for oxygen delivery. Int J Pharm 381(2):160–165

Dash RK, Bassingthwaighte JB (2010) Erratum to: blood HbO_2 and $HbCO_2$ dissociation curves at varied O_2, CO_2, pH, 2,3-DPG and temperature levels. Ann Biomed Eng 38(4):1683–1701

Dennery PA (2010) Oxygen administration in the care of neonates: a double-edged sword. Chin Med J 123(20):2938–2942

Dijkmans PA, Juffermans LJ, Musters RJ, van Wamel A, ten Cate FJ, van Gilst W, Visser CA, de Jong N, Kamp O (2004) Microbubbles and ultrasound: from diagnosis to therapy. Eur J Echocardiogr 5(4):245–256

Donovan L, Welford SM, Haaga J, LaManna J, Strohl KP (2010) Hypoxia: implications for pharmaceutical developments. Sleep Breath 14(4):291–298

Ferrara KW, Borden MA, Zhang H (2009) Lipid-shelled vehicles: engineering for ultrasound molecular imaging and drug delivery. Acc Chem Res 42(7):881–892

Goutelle S, Maurin M, Rougier F, Barbaut X, Bourguignon L, Ducher M, Maire P (2008) The Hill equation: a review of its capabilities in pharmacological modeling. Fundam Clin Pharmacol 22(6):633–648

Guo S, DiPietro LA (2010) Factors affecting wound healing. J Dent Res 89(3):219–229

Juffermans LJ, Dijkmans PA, Musters RJ, van Wamel A, Bouakaz A, ten Cate FJ, Deelman L, Visser CA, de Jong N, Kamp O (2004) Local drug and gene delivery through microbubbles and ultrasound: a safe and efficient alternative for viral vectors? Neth Heart J 12(9):394–399

Juffermans LJ, Dijkmans PA, Musters RJ, Visser CA, Kamp O (2006) Transient permeabilization of cell membranes by ultrasound-exposed microbubbles is related to formation of hydrogen peroxide. Am J Physiol Heart Circ Physiol 291(4):H1595–H1601

Kulikovsky M, Gil T, Mattanes I, Karmeli R, Har-Shai Y (2009) Hyperbaric oxygen therapy for non-healing wounds. Isr Med Assoc J 11(8):480–485

Kurup N, Naik P (2010) Microbubbles, A novel delivery system. J Pharmaceut Res Health Care 2(3):228–234

Lapotko D (2011) Plasmonic nanobubbles as tunable cellular probes for cancer theranostics. Cancers 3(1):802–840

Qin S, Caskey CF, Ferrara KW (2009) Ultrasound contrast microbubbles in imaging and therapy: physical principles and engineering. Phys Med Biol 54(6):R27–R57

Raoof S, Goulet K, Esan A, Hess DR, Sessler CN (2010) Severe hypoxemic respiratory failure: part2-nonventilatory strategies. Chest 137(6):1437–1448

Scholz AW, Eberle B, Heussel CP, David M, Schmittner MD, Quintel M, Schreiber LM, Weiler N (2010) Ventilation-perfusion ratio in Perflubron during partial liquid ventilation. Anesth Analg 110(6):1661–1668

Swanson EJ, Mohan V, Kheir J, Borden MA (2010) Phospholipid-stabilized microbubble foam for injectable oxygen delivery. Langmuir 26(20):15726–15729

Takahashi M (2005) The 1 potential of microbubbles in aqueous solutions, Electrical property of the gas-water interface. J Phys Chem B 109(46):21858–21864

Takahashi M, Kawamura T, Yamamoto Y, Ohnari H, Himuro S, Shakutsui H (2003) Effect of shrinking microbubble on gas hydrate formation. J Phys Chem B 107(10):2171–2173

Takahashi M, Chiba K, Li P (2007) Free-radical generation from collapsing microbubbles in the absence of a dynamic stimulus. J Phys Chem B 111(6):1343–1347

Taylor CT, Moncada S (2010) Nitric oxide, cytochrome C oxidase, and the cellular response to hypoxia. Arterioscler Thromb Vasc Biol 30(4):643–647

12 3

Wang C, Zhang X, Liu F, Paule MG, Slikker W Jr (2010) Anesthetic-induced oxidative stress and potential protection. Sci World J 10:1473–1482

Ward DS, Karan SB, Pandit JJ (2011) Hypoxia: developments in basic science, physiology and clinical studies. Anaesthesia 66(Suppl 2):19–26

Xu Q, Nakajima M, Liu Z, Shiina T (2011) Biosurfactants for microbubble preparation and application. Int J Mol Sci 12(1):462–475

Regulatory mode shift of Tbc1d1 is required for acquisition of insulin-responsive GLUT4-trafficking activity

Hiroyasu Hatakeyama[a] and Makoto Kanzaki[a,b]
[a]Graduate School of Biomedical Engineering, Tohoku University, Sendai, Miyagi 980-8579, Japan; [b]Core Research for Evolutional Science and Technology, Japan Science and Technology Agency, Tokyo 102-0075, Japan

ABSTRACT **Tbc1d1 is key to skeletal muscle GLUT4 regulation. By using GLUT4 nanometry combined with a cell-based reconstitution model, we uncover a shift in the regulatory mode of Tbc1d1 by showing that Tbc1d1 temporally acquires insulin responsiveness, which triggers GLUT4 trafficking only after an exercise-mimetic stimulus such as aminoimidazole carboxamide ribonucleotide (AICAR) pretreatment. The functional acquisition of insulin responsiveness requires Ser-237 phosphorylation and an intact phosphotyrosine-binding (PTB) 1 domain. Mutations in PTB1, including R125W (a natural mutant), thus result in complete loss of insulin-responsiveness acquisition, whereas AICAR-responsive GLUT4-liberation activity remains intact. Thus our data provide novel insights into temporal acquisition/memorization of Tbc1d1 insulin responsiveness, relying on the PTB1 domain, possibly a key factor in the beneficial effects of exercise on muscle insulin potency.**

Monitoring Editor
Adam Linstedt
Carnegie Mellon University

Received: Oct 9, 2012
Revised: Jan 4, 2013
Accepted: Jan 8, 2013

INTRODUCTION

Insulin and exercise are two important physiological stimuli of GLUT4 translocation from its intracellular storage compartment(s) to the cell surface (Goodyear and Kahn, 1998). The upstream signaling pathways of these two stimuli differ from each other: insulin's actions are mediated by phosphatidylinositol 3-kinase/Akt, whereas exercise might involve AMP-activated protein kinase (AMPK). Therefore these two biochemical signaling pathways should converge somewhere in order to be deciphered into the physical process of GLUT4 translocation. Recent studies suggest that two tre-2/USP6, BUB2, cdc16 domain (Tbc1d)–family Rab GTPase–activating proteins (RabGAPs)—the Akt substrate of 160 kDa (AS160)/Tbc1d4 (hereafter AS160) and Tbc1d1—act as convergence sites for insulin- and exercise-responsive GLUT4 translocation. These proteins share ~50% identical amino acid sequences with similar domain structures, such as two phosphotyrosine-binding (PTB) domains, a putative calmodulin-binding domain (CBD), a RabGAP domain (Roach *et al.*, 2007; Park *et al.*, 2011), and multiple Akt-phosphorylation sites (Sano *et al.*, 2003; Peck *et al.*, 2009). The substrate specificities of these RabGAPs in vitro are also similar. One notable difference between these two proteins is tissue distribution: AS160 is expressed in multiple tissues at similar levels, whereas Tbc1d1 is highly expressed in skeletal muscle as compared with other tissues (Taylor *et al.*, 2008; Castorena *et al.*, 2011). Another key difference is the presence of an AMPK-phosphorylation site (Ser-237) in Tbc1d1 (Nedachi *et al.*, 2008; Taylor *et al.*, 2008; Vichaiwong *et al.*, 2010), which apparently contributes to the unique regulatory aspects of Tbc1d1, such as contraction-induced glucose uptake. Studies such as these have provided a detailed understanding of the biochemical properties of AS160 and Tbc1d1, but the functional aspects of these proteins remain ambiguous due to the technical limitations of traditional biochemical assays for analyzing GLUT4 trafficking, which can assess only cell surface amounts of GLUT4 and cannot directly describe intracellular GLUT4 behavior.

This article was published online ahead of print in MBoC in Press (http://www.molbiolcell.org/cgi/doi/10.1091/mbc.E12-10-0725) on January 16, 2013.

Address correspondence to: Makoto Kanzaki (kanzaki@bme.tohoku.ac.jp).

Abbreviations used: AM, acetoxymethyl; AMPK, AMP-activated protein kinase; AS160, Akt substrate of 160 kDa; $[Ca^{2+}]_i$, intracellular Ca^{2+} concentration; CBD, calmodulin-binding domain; IRAP, insulin-responsive aminopeptidase; LRP1, low-density-lipoprotein receptor–related protein 1; MSD, mean-square displacement; NPE, *o*-nitrophenyl ethylene glycol tetraacetic acid; PTB, phosphotyrosine binding; QD, quantum dot; RabGAP, Rab GTPase-activating protein; Tbc1d, tre-2/UPS6, BUB2, cdc16 domain.

© 2013 Hatakeyama and Kanzaki. This article is distributed by The American Society for Cell Biology under license from the author(s). Two months after publication it is available to the public under an Attribution–Noncommercial–Share Alike 3.0 Unported Creative Commons License (http://creativecommons.org/licenses/by-nc-sa/3.0).

"ASCB®," "The American Society for Cell Biology®," and "Molecular Biology of the Cell®" are registered trademarks of The American Society of Cell Biology.

Supplemental Material can be found at:
http://www.molbiolcell.org/content/suppl/2013/01/14/mbc.E12-10-0725.DC1.html

To overcome the methodological limitations, we recently developed a novel nanometrological method for quantifying intracellular GLUT4 behavior based on single-molecule imaging with quantum dot (QD) fluorescent nanocrystals, which can dissect the intracellular GLUT4-trafficking process into discrete, experimentally traceable steps (Fujita *et al.*, 2010; Hatakeyama and Kanzaki, 2011). With this approach, we revealed the "static retention" property governed by sortilin to be the major sequestration mechanism for GLUT4 (Hatakeyama and Kanzaki, 2011). Moreover, we clearly identified insulin-responsive "liberation" of static GLUT4 as a major functional aspect of insulin action and also demonstrated that AS160 governed this process in an Akt-mediated phosphorylation-dependent manner (Fujita *et al.*, 2010). Of importance, by virtue of our GLUT4 nanometry, we successfully established an "experimental reconstitution model" of mature insulin-responsive GLUT4 trafficking systems in 3T3L1 fibroblasts by exogenously expressing only two proteins—sortilin and AS160. This cell-based reconstitution model has contributed to analyzing regulatory mechanisms of intracellular GLUT4 behavior in further detail by focusing on specific trafficking processes, which cannot be done with traditional biochemical assays.

Unlike AS160, the functional roles of its closest relative, Tbc1d1, remain uncertain. A major obstacle in Tbc1d1 functional research is its predominant expression in skeletal muscles, making it difficult to investigate GLUT4 regulation. Revealing Tbc1d1 function would presumably be important for understanding both physiological and pathophysiological glucose homeostasis, since the R125W mutation of Tbc1d1 can cause severe obesity (Stone *et al.*, 2006; Meyre *et al.*, 2008), and this mutation reportedly decreases insulin-dependent glucose transport (An *et al.*, 2010). Therefore, in the present study, by using GLUT4 nanometry combined with a cell-based experimental reconstitution model, we examine the functional roles of Tbc1d1 in great detail, focusing especially on GLUT4-liberation processes. Our findings reveal a unique memorization ability for insulin-responsive activity, relying on the PTB1 domain of Tbc1d1. This might explain the defect caused by natural mutations such as R125W.

RESULTS

Tbc1d1 serves as a key regulator of aminoimidazole carboxamide ribonucleotide–induced GLUT4 liberation

With QD-based GLUT4 nanometry, we can track the movements of individual intracellular GLUT4 molecules with high precision (Figure 1, A and B). Using this approach, we describe intracellular GLUT4 behavior based on two parameters—velocities and representative diffusion coefficient maps (Figure 1, C–E). The calculations of these values were performed as previously described (Fujita *et al.*, 2010; Hatakeyama and Kanzaki, 2011; see *Materials and Methods*). Note that rightward shift of the velocity distribution or increases in spots having hotter colors in representative diffusion coefficient maps indicate increases in fast-moving molecules. With this approach, we reconfirmed that the static GLUT4 storage compartment was generated by exogenous sortilin expression and found that the resulting stationary GLUT4 behavior was not influenced by additional coexpression of Tbc1d1, whereas expression of Tbc1d1 alone generated no static GLUT4 storage compartment (Figure 1F and Supplemental Figure S1A). Because the calculated velocities are "apparent" values representing a combination of true movement and inevitable instrumental noise, instead of raw data we use the "corrected" velocities, obtained by subtracting apparent velocities in fixed cells in the figures, to represent mean velocities (see *Materials and Methods*).

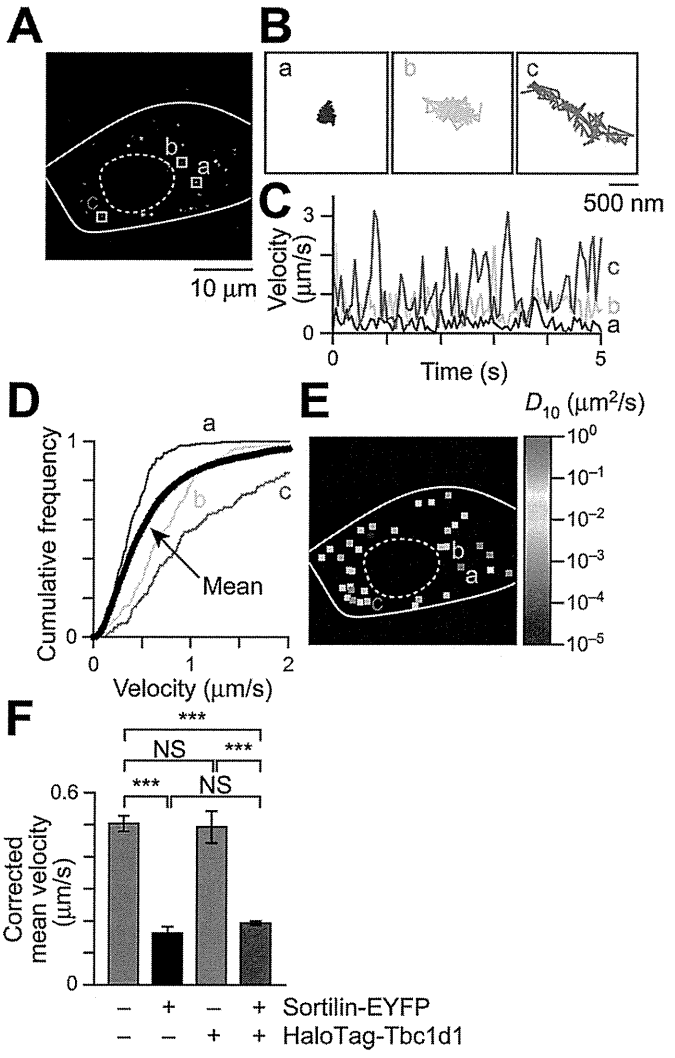

FIGURE 1: Intracellular GLUT4 nanometry based on single-molecule imaging. (A) Snapshot of QD fluorescence in 3T3L1 fibroblasts. Trajectories (B), velocity vs. time plots (C), and cumulative velocity distributions (D) of three particles shown in A. In D, the mean velocity distribution calculated from all particles in the cell is also shown (black), with error bars omitted for clarity. Mean velocities (in μm/s) of the three particles shown in A are 0.38 (a), 0.50 (b), and 1.13 (c), and the mean velocity of all particles within the cell is 0.62 μm/s. (E) Diffusion coefficient (D_{10}) map in a cell shown in A. The three particles shown in A are also indicated. Right, pseudocolor coding used to represent the diffusion coefficients of the molecules estimated by linear fitting of MSD values (see *Materials and Methods*). (F) Mean velocities in cells expressing the indicating proteins. The values were obtained from 6–84 cells. ***$p < 0.001$ by Tukey–Kramer multiple comparison.

Using fibroblasts exogenously expressing both sortilin and Tbc1d1 (Supplemental Figure S1E), we first analyzed insulin effects and found that insulin failed to liberate GLUT4 from its static state (Figure 2, A and D), which differed from the response of fibroblasts expressing sortilin and AS160 (Hatakeyama and Kanzaki, 2011). Instead, AMPK activators, either aminoimidazole carboxamide ribonucleotide (AICAR) or A-769642, induced GLUT4 liberation, displaying rightward shift of the velocity distribution and increases in spots with hotter colors in diffusion coefficient maps (Figure 2, B and D, and Supplemental Figure S1B; see also Figure 3H), along with increased phosphorylation of Ser-237 (AMPK site),

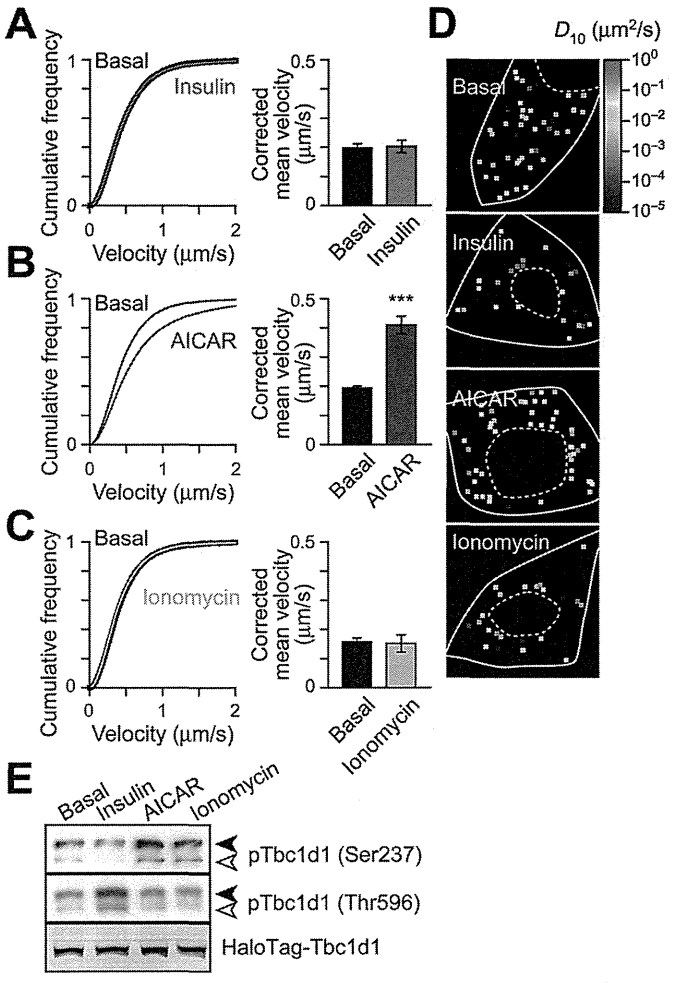

FIGURE 2: Tbc1d1 mediates AICAR-dependent GLUT4 liberation. Velocity distributions (left) and corrected mean velocities (right) of GLUT4 movement (A) before (black) and after (red) insulin stimulation (100 nM, 30 min, $n = 12$), (B) without (black, $n = 67$) or with (blue, $n = 39$) AICAR (1 mM, 30 min), and (C) before (black) and after (cyan) ionomycin treatment (0.1 μg/ml, 10 min, $n = 4$). ***$p < 0.001$. (D) Representative diffusion coefficient maps of GLUT4 movement in cells under the indicated conditions. (E) Tbc1d1 phosphorylation induced by insulin (100 nM, 5 min), AICAR (1 mM, 30 min), or ionomycin (0.1 μg/ml, 5 min). Solid and open arrowheads represent exogenously expressed HaloTag-Tbc1d1 and endogenous Tbc1d1, respectively. Exogenously expressed HaloTag-Tbc1d1 was also detected by labeling with fluorescent HaloTag ligand.

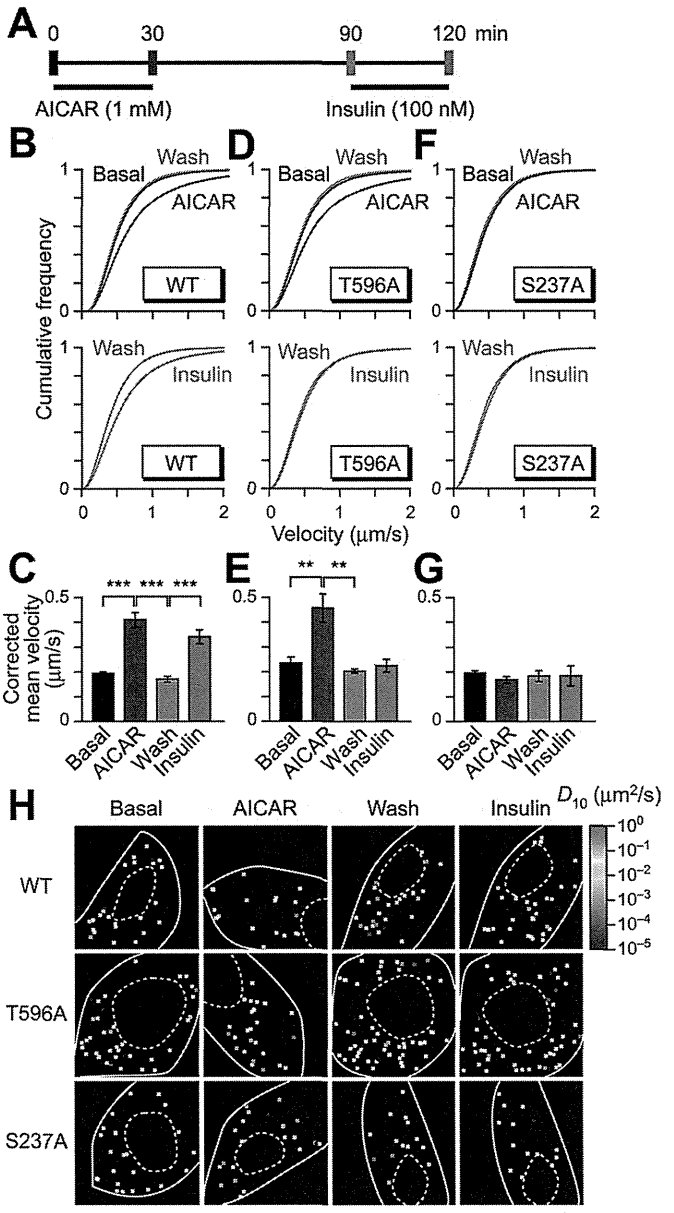

FIGURE 3: Acquisition of insulin responsiveness of Tbc1d1 by sequential treatment with AICAR and insulin. (A) Treatment protocol. Imaging was performed at the times indicated by vertical bars. Mean velocity distributions (B, D, and F) and corrected mean velocities (C, E, and G) of GLUT4 movement in cells expressing wild-type (B, C), T596A (D, E), and S237A (F, G) Tbc1d1. In B and C, the data in basal and AICAR-treated cells are the same as in Figure 2B. Data were obtained from at least three cells. **$p < 0.01$, ***$p < 0.001$. Statistical analyses were performed with Tukey–Kramer multiple comparison. (H) Representative diffusion coefficient maps of GLUT4 movement in cells under the indicated conditions.

but not with that of Thr-596 (Akt site; Figure 2E). In contrast, insulin increased Thr-596, but not Ser-237, phosphorylation (Figure 2E). We also found that a forced increase of intracellular Ca^{2+} concentration ($[Ca^{2+}]_i$) by ionomycin induced no significant GLUT4 liberation (Figure 2, C and D), despite this treatment augmenting phosphorylation of Ser-237 but not Thr-596 (Figure 2E) as in AICAR-treated cells. AICAR-induced GLUT4 liberation was dependent on exogenously expressed Tbc1d1, as there was no liberation in fibroblasts expressing sortilin alone (Supplemental Figure S1C). Consistent with our previous observations (Hatakeyama and Kanzaki, 2011), insulin also failed to liberate static GLUT4 in these fibroblasts (Supplemental Figure S1D). These results indicate that fibroblasts have no functionally significant expression of either AS160 or Tbc1d1, at least in terms of GLUT4-liberation activity.

Tbc1d1 acquires its insulin-responsive GLUT4-liberation ability after AICAR pretreatment

We next examined whether sequential multiple stimuli liberated GLUT4 in a Tbc1d1-dependent manner (Figure 3A). Intriguingly, we found that, although insulin alone failed to release static GLUT4 as noted earlier (Figure 2A), insulin did trigger GLUT4 liberation when Tbc1d1-expressing cells had been treated previously with AICAR (Figure 3, B, C, and H). The static GLUT4 behavior was restored at 1 h after AICAR removal (Figure 3, B, C, and H), presumably due to

sortilin-mediated retrograde trafficking of GLUT4 (Hatakeyama and Kanzaki, 2011). Although the static characteristics of their GLUT4-inducing behaviors were indistinguishable, insulin displayed a potent ability to liberate GLUT4 only in the AICAR-exposed requiescent cells (Figure 3, B, C, and H; cf. Figure 2A), and this insulin action was still observed even 3 h after AICAR withdrawal (unpublished data). Acquired insulin responsiveness was abolished by wortmannin, a phosphatidylinositol 3-kinase inhibitor (Supplemental Figure S2), and a Tbc1d1/T596A mutant displayed no insulin-responsive GLUT4 liberation (Figure 3, D, E, and H). However, this mutant was fully functional in terms of introductory AICAR-induced GLUT4 liberation (Figure 3, D, E, and H).

On the other hand, a Tbc1d1/S237A mutant completely lacked GLUT4-liberation activity regardless of the stimuli used, including combinatorial (Figure 3, F–H), indicating phosphorylation of Ser-237 to be crucial not only for AICAR-dependent GLUT4 liberation, but also for AICAR-induced temporal acquisition of insulin-responsive activity. We confirmed that AICAR-induced Ser-237 phosphorylation was restored to basal levels 1 h after AICAR removal and that insulin-induced Thr-596 phosphorylation was not significantly influenced by AICAR treatment (Figure 4). In addition, mutational analysis of other potential phosphorylation sites around the crucial Thr-596, including Ser-565 and Ser-566 (Peck *et al.*, 2009), demonstrated that these serine residues are irrelevant to GLUT4-liberation activity (unpublished data), although the possibility that other phosphorylation sites are involved cannot be ruled out. It should be noted that the acquisition of insulin responsiveness was observed in the Tbc1d1-expressing fibroblasts treated with AS160 siRNA (Supplemental Figure S3).

Taken together, the results indicate that phosphorylation processes of both Ser-237 and Thr-596, even if sequential rather than simultaneous, appeared to be crucial for acquiring insulin-responsive activity. More specifically, phosphorylation of Ser-237 was essential for endowing Tbc1d1 with insulin responsiveness, whereas subsequent insulin-induced GLUT4 liberation required phosphorylation of Thr-596, but not Ser-237, under these specific conditions.

Repackaging into a distinct GLUT4-storage compartment is not necessary for insulin responsiveness

Tbc1d1 appears to become insulin responsive in certain situations. However, given that the initial AICAR treatment liberates GLUT4, resulting in its drastic redistribution, it is possible that after AICAR withdrawal the released GLUT4 was restored to a distinct compartment, one with the insulin-responsive property, different from that one in which GLUT4 was originally localized. Alternatively, it is also possible that Tbc1d1 somehow acquired insulin responsiveness after AICAR treatment. To address this important question, we showed that insulin was also capable of triggering Tbc1d1-dependent GLUT4 liberation when $[Ca^{2+}]_i$ was temporally or simultaneously increased. For rapid and transient increases in $[Ca^{2+}]_i$, we applied photolysis of caged Ca^{2+} compound *o*-nitrophenyl ethylene glycol tetraacetic acid (NPE)–loaded cells (Figure 5A). The increases in $[Ca^{2+}]_i$ alone failed to liberate GLUT4 at least for 10 min (Figure 5B), whereas with insulin, acute increases in $[Ca^{2+}]_i$ released GLUT4 just 30 s after photolysis (Figure 5C, $p < 0.001$ by Kolmogorov–Smirnov test). Similarly, immediately after increases in $[Ca^{2+}]_i$, insulin stimulation liberated GLUT4 in wild type–expressing cells (Figure 5D) but not in T596A or S237A mutant cells (Supplemental Figure S4, A and B). The effect of $[Ca^{2+}]_i$ in causing Tbc1d1 insulin responsiveness lasted for 5 min, and the insulin gradually lost this ability (Supplemental Figure S4, C and D). Ionomycin showed no significant changes in insulin-induced phosphorylation of Tbc1d1 (Supplemental Figure S4E).

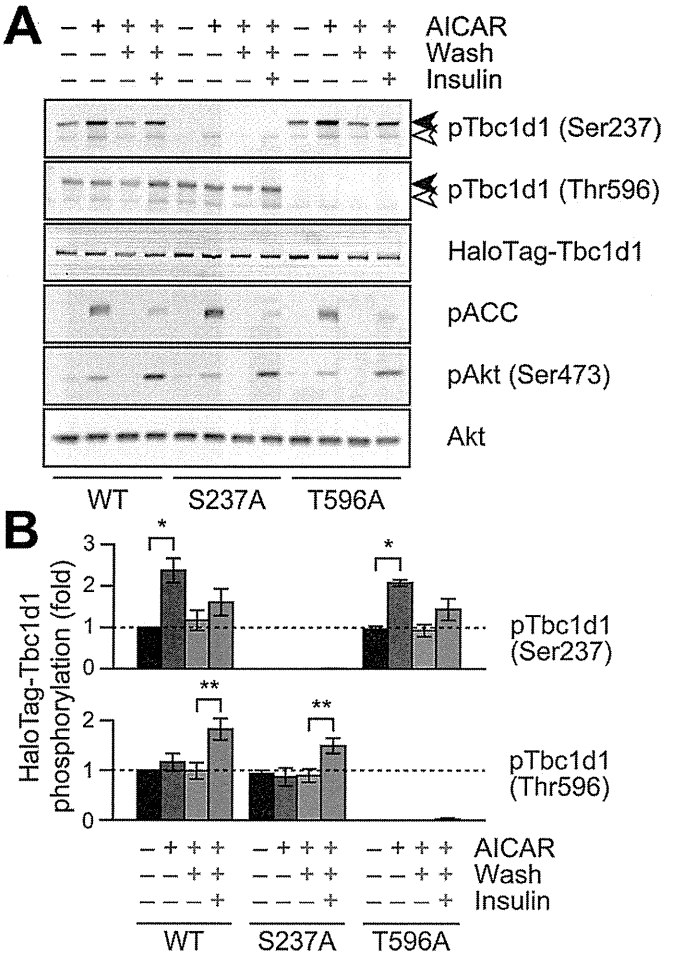

FIGURE 4. Effects of Tbc1d1 mutants on AICAR- or insulin-induced phosphorylation. Representative Western blotting (A) and quantification (B) of HaloTag-Tbc1d1 phosphorylation. In A, pACC and pAkt are also shown in order to confirm the activations of AMPK and insulin signaling pathways. In B, the values were calculated from three independent assays. The data are shown as ratios (phosphorylation/total) and as fold increases compared with untreated wild type. $^*p < 0.05$, $^{**}p < 0.01$.

These observations show that drastic GLUT4 repackaging is not always necessary to endow insulin-responsive Tbc1d1 activity, although AICAR pretreatment endowed Tbc1d1 with much longer potency than did $[Ca^{2+}]_i$ transients. Similar to AICAR-exposed cells, phosphorylation sites of both Ser-237 (AMPK site) and Thr-596 (Akt site) were crucial for generating the temporal insulin-responsive Tbc1d1 activity. It is intriguing, however, that Tbc1d1/W725G, a mutant version of the putative CBD in which AS160 possesses a similar CBD (Kane and Lienhard, 2005), exhibited no obvious defect (unpublished data), suggesting that the CBD was minimally involved, at least under these experimental conditions.

Temporal endowment of insulin-responsive potency requires intact PTB domain

Our GLUT4 nanometry monitoring of intracellular behaviors of single GLUT4 molecules provided compelling evidence that Tbc1d1 does indeed function as a key nexus deciphering biochemical phosphorylation events of Ser-237 and Thr-596, with multiple, even sequential, stimuli being involved in the physical process of GLUT4 liberation. However, our finding that their phosphorylation did not

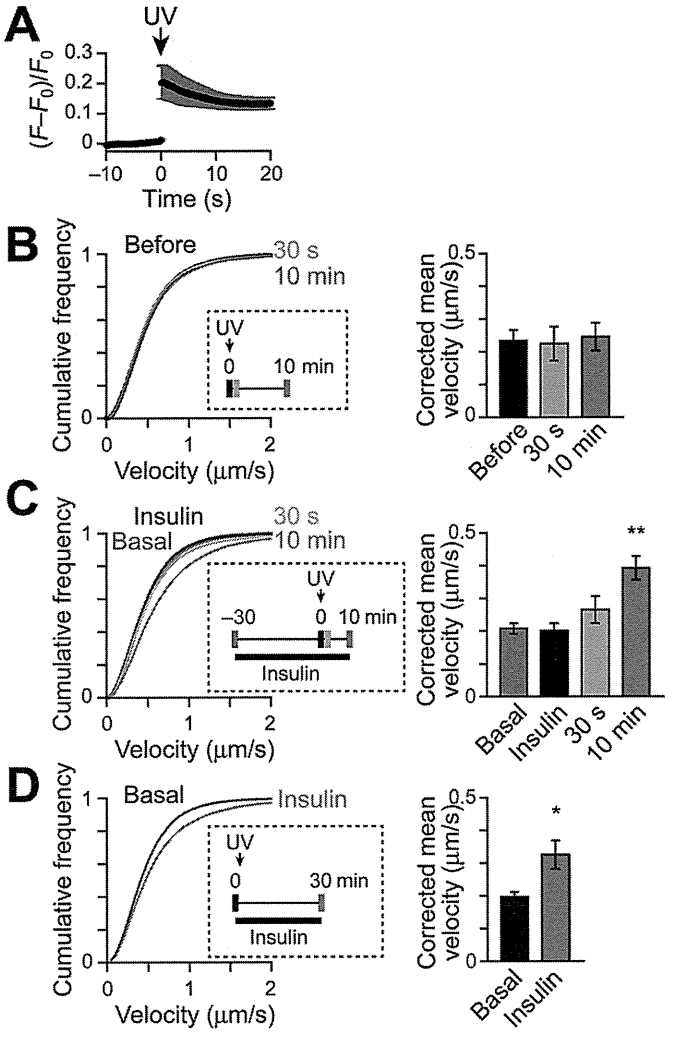

FIGURE 5: Acquisition of insulin responsiveness of Tbc1d1 by combined stimulation with Ca^{2+} and insulin. (A) Changes in $[Ca^{2+}]_i$ induced by NPE photolysis in cells monitored by Ca^{2+} indicator fluo-4 fluorescence (F). Photolysis was induced at time 0 (UV, arrow). F_0 represents mean fluorescence intensity before photolysis. Velocity distributions (left) and corrected mean velocities (right) of GLUT4 movement (B) before (black) and after (orange: 30 s; red: 10 min) NPE photolysis ($n = 6$), (C) basal (gray), insulin-stimulated (black), and after (orange: 30 s; red: 10 min) photolysis ($n = 7$), and (D) before (black) and after (red) insulin stimulation (100 nM, $n = 6$). Insets show detailed treatment and acquisition protocols. *$p < 0.05$ and ** $p < 0.01$ by Dunnett's multiple comparison vs. basal.

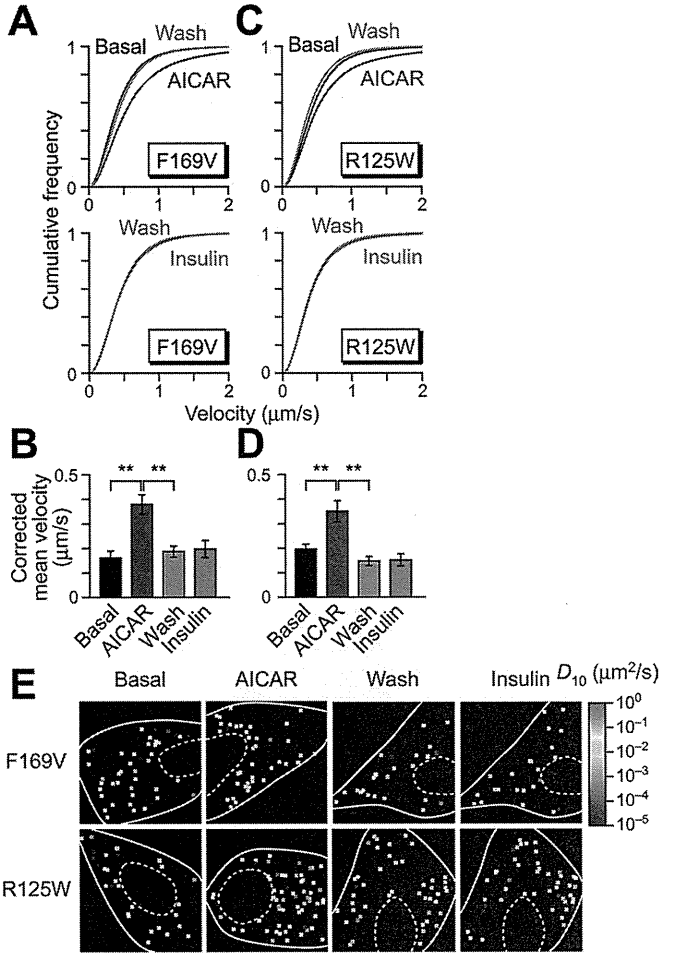

FIGURE 6: Intact PTB1 domain is necessary for temporal acquisition of insulin responsiveness. Sequential stimulation with AICAR and insulin in cells expressing F169V (A, B) and R125W (C, D). Stimulation protocols and colors are the same as in Figure 3. Data were obtained from at least four cells. **$p < 0.01$. Statistical analyses were performed with Tukey–Kramer multiple comparison. (E) Representative diffusion coefficient maps of GLUT4 movement in cells under indicated conditions.

always need to be simultaneous to exert full liberation activity was rather surprising since phosphorylated Thr-596 alone, unlike phosphorylated Ser-237, was reportedly insufficient for 14-3-3 binding (Chen *et al.*, 2008; Pehmoller *et al.*, 2009), and previous studies on AS160 showed the importance of 14-3-3 association in GLUT4 regulation (Ramm *et al.*, 2006; Chen *et al.*, 2011; Koumanov *et al.*, 2011).

To further explore molecular mechanisms underlying temporal endowment of insulin responsiveness, we attempted to identify responsible Tbc1d1 domain(s), other than these key phosphorylation sites, that might be involved in functional acquisition/memorization enabling Tbc1d1 insulin responsiveness. Mutational analysis of several major domains in Tbc1d1 revealed that the functional PTB domain is essential, since a point mutation in the putative PTB sequence in Tbc1d1 (Tbc1d1/F169V), believed to interact with NPxY asparagine (Zhou *et al.*, 1995), showed no acquired ability to liberate GLUT4 in response to sequential insulin stimulation, despite introductory AICAR-dependent GLUT4 liberation being accomplished (Figure 6, A, B, and E). Insulin-responsive GLUT4 liberation with a combined $[Ca^{2+}]_i$ transient was also impaired in the Tbc1d1/F169V mutant (Supplemental Figure S5, A and B). We also found that a natural mutation (R125W) in the same PTB domain of Tbc1d1 (Stone *et al.*, 2006; Meyre *et al.*, 2008) exhibits essentially the same defects in acquisition/memorization of insulin-responsive ability after AICAR-pretreatment as with the combinatorial increase of $[Ca^{2+}]_i$ (Figure 6, C–E, and Supplemental Figure S5). Tbc1d1 phosphorylation profiles at Ser-237 and Thr-596 did not differ significantly among these mutants and wild type (Figure 7).

Taken together, these data provide important insights into a unique regulatory mechanism of Tbc1d1 that relies on an intact PTB1 domain, which is essential for Ser-237 phosphorylation–dependent acquisition of insulin responsiveness with AICAR pretreatment.

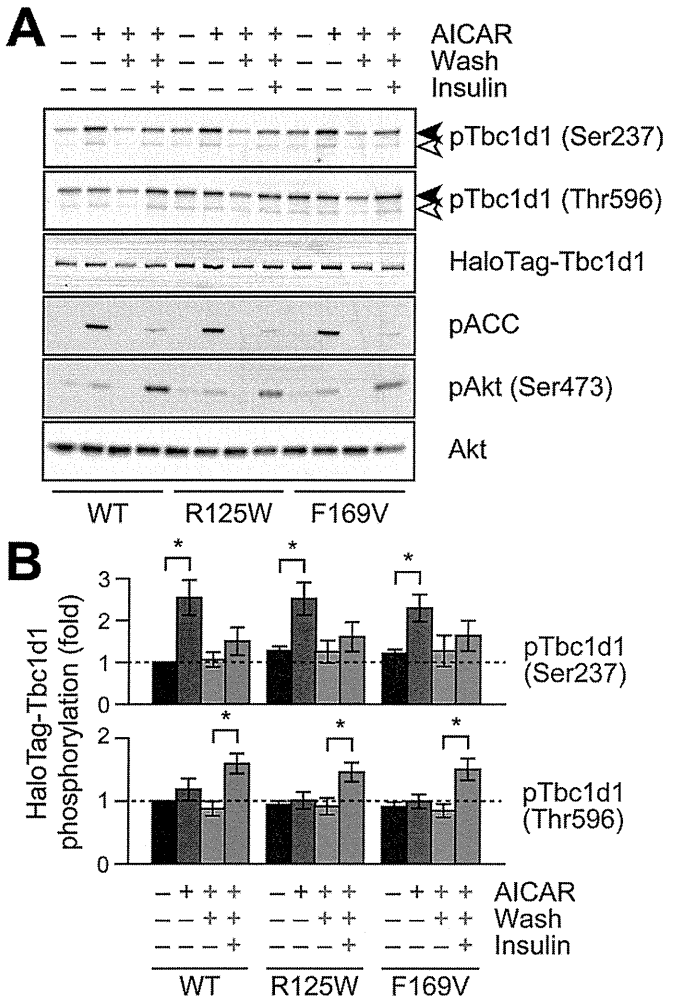

FIGURE 7: Effects of Tbc1d1 PTB1-domain mutants on AICAR- and insulin-induced phosphorylation. Representative Western blotting (A) and quantification (B) of HaloTag-Tbc1d1 phosphorylation. Data were obtained and represented as in Figure 4. *$p < 0.05$.

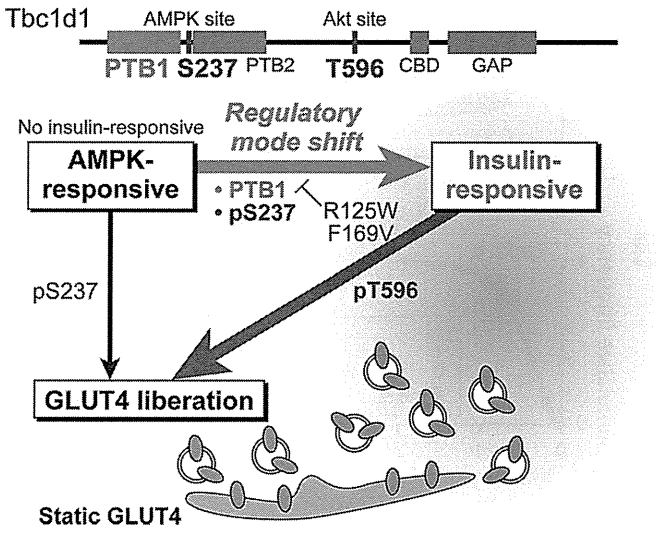

FIGURE 8: Schematic depiction of the shift in regulatory mode of Tbc1d1. Tbc1d1 is required for AICAR-dependent GLUT4 liberation from the static GLUT4 storage compartment. Whereas naive Tbc1d1 has no ability to respond to the initial insulin stimulation, Tbc1d1 acquires insulin responsiveness only after exposure to exercise-mimetic stimuli. This shift in regulatory mode of Tbc1d1 for GLUT4 liberation requires Ser-237 phosphorylation and the PTB1 domain. PTB1-domain mutants including R125W and F169V exhibit no regulatory mode shift and thus no insulin responsiveness.

DISCUSSION

Our GLUT4 nanometry, combined with a cell-based experimental reconstitution model, allowed the clear demonstration of Tbc1d1 function and its unique regulatory mechanisms in GLUT4 liberation (Figure 8). Our findings provide novel mechanistic insights into the regulatory mode shift of Tbc1d1 and conceptual frameworks for understanding insulin-responsive GLUT4 translocation involving Tbc1d1, as in skeletal muscle, where Tbc1d1 is abundantly expressed (Castorena *et al.*, 2011). It is noteworthy that mutations in the PTB1 domain, including R125W, result in complete loss of the acquisition of insulin responsiveness, which may explain the defect identified in human patients with this natural mutation (Stone *et al.*, 2006; Meyre *et al.*, 2008) and also suggests that this regulatory mode shift resulting in the acquisition of insulin responsiveness after exercise-mimetic stimuli is related to the beneficial effects of exercise on muscle insulin potency, particularly augmented GLUT4 translocation.

Superiority of GLUT4 nanometry for analyzing Tbc1d1 functions

Two significant advantages of our experimental approach contribute to such clear determinations of functional roles of Tbc1d1. First, our experimental reconstitution model can definitively describe the actions of specific regulatory factors that are inherently up-regulated only upon cellular differentiation, that is, sortilin and Tbc1d-family RabGAPs, for GLUT4 trafficking by manipulating ectopic expression levels or combinations of these key factors in undifferentiated fibroblastic cells (Hatakeyama and Kanzaki, 2011). On the contrary, due to various technical limitations, previous studies attempting to understand functional aspects of Tbc1d1 in GLUT4 translocation, which used a cell-surface GLUT4 exposure assay, were performed in mature 3T3L1 adipocytes overexpressing exogenous Tbc1d1 (Roach *et al.*, 2007; Chavez *et al.*, 2008), making it difficult to exclusively examine the functional roles of Tbc1d1 versus those of AS160 despite detailed knowledge of their biochemical properties. Second, our single-molecule imaging system can dissect complex GLUT4 trafficking itineraries in each experimentally traceable step, including liberation, transport, and tethering/fusion with the plasma membrane (Fujita *et al.*, 2010).

We focused on the stimulus-responsive liberation of GLUT4 from the static compartment because of the similar functional context of Tbc1d1 with AS160, which is required for insulin-responsive liberation. Although the possibility of Tbc1d1 being involved in other GLUT4-trafficking processes cannot be ruled out, the liberation process must be critical for the entire GLUT4 itinerary since liberation from the static compartment is indispensable for GLUT4 to reach the plasma membrane.

One striking observation in the present study is that Tbc1d1 itself, unaccompanied by AS160, can function similarly to AS160, facilitating GLUT4 liberation, although their proximal regulatory signals differ. Tbc1d1 can facilitate GLUT4 liberation in response to AICAR treatment. As expected, AICAR-induced Ser-237 phosphorylation was found to be important, whereas insulin-induced Thr-596 phosphorylation was insufficient for GLUT4 liberation, possibly due to failure of 14-3-3 binding to solely phosphorylated Thr-596

(Chen *et al.*, 2008). However, a key unexpected observation was failure of GLUT4 liberation by ionomycin despite obvious phosphorylation of Tbc1d1 at Ser-237, implying a further layer of complexity in Tbc1d1 regulation, apparently involving mechanisms unrelated or parallel to Ser-237 phosphorylation (as discussed in detail later).

Regulatory mode shift of Tbc1d1

To our surprise, Tbc1d1 acquires temporal insulin-responsive ability for GLUT4 liberation only after exercise-mimetic stimuli such as AICAR pretreatment. This observation strongly suggested that Tbc1d1 molecules have at least two distinct regulatory modes (AMPK responsive and insulin responsive) and that Tbc1d1 undergoes the regulatory mode shift in response to a Ser-237 phosphorylation process, even though this phosphorylation is not necessarily persistent (Figure 8). Of greater importance, we found the necessity of the PTB1 domain of Tbc1d1 for its shift of regulatory mode by taking advantage of Tbc1d1 being phosphorylated by two distinct inputs governed by different protein kinases (AMPK and Akt).

Both AS160 and Tbc1d1 have two PTB domains, which are classified as disabled like (Uhlik *et al.*, 2005). A truncation mutant in AS160 (R363X) has been identified as being involved in postprandial hyperinsulinemia (Dash *et al.*, 2009), and a recent report demonstrated overexpression of the PTB-domain fragments of AS160 to affect 14-3-3 binding and in vitro fusion activities of GLUT4 vesicles (Koumanov *et al.*, 2011), highlighting the importance of PTB domains. Thus AS160 might also have a similar regulatory mechanism involving PTB domains, although both crucial phosphorylation sites of AS160 are governed by Akt and thus have yet to be discovered. In any case, the regulatory mode shift of Tbc1d1 was found to be dependent on the PTB1 domain, and malfunction in this regulatory mode shift might be rather widely involved in human pathophysiological states such as insulin resistance and type 2 diabetes, as exemplified by the aforementioned genetic disorders.

In general, PTB domains are adaptors or scaffolds for proteins to recruit signaling complexes by binding with NPxY motifs in both phosphotyrosine-dependent and -independent manners (Uhlik *et al.*, 2005). Low-density-lipoprotein receptor–related protein 1 (LRP1), a recently identified component of GLUT4-containing vesicles (Jedrychowski *et al.*, 2010), has two NPxY motifs in its C-terminal cytoplasmic domain and reportedly binds with PTB domain–containing proteins such as ShcA, Fe65, and disabled-like ones (Stolt and Bock, 2006). In 3T3L1 adipocytes, knockdown of LRP1 resulted in reduced GLUT4 expression and decreased insulin-stimulated glucose uptake, suggesting the importance of LRP1 in appropriate GLUT4 behavior. In addition, the cytoplasmic region of LRP1 has the ability to bind with AS160 by glutathione *S*-transferase pull down (Jedrychowski *et al.*, 2010). Therefore we analyzed the possibility of the LRP1 cytoplasmic region being a binding partner of Tbc1d1 PTB domains. However, our preliminary results suggest that the cytoplasmic region of LRP1 may not be a major regulator for Tbc1d1 actions since the cytoplasmic region of LRP1 shows neither detectable binding with Tbc1d1 nor augmented tyrosine phosphorylation in response to various stimuli, including AICAR and insulin. Furthermore, overexpression of the cytoplasmic region of LRP1 lacking a luminal domain failed to modify any GLUT4 behaviors under basal or various stimulated conditions (unpublished observations). Insulin-regulated aminopeptidase (IRAP) is another major constituent of GLUT4-containing vesicles and is reported to be a binding partner of AS160 PTB domain–containing regions (Larance *et al.*, 2005; Peck *et al.*, 2006; Park *et al.*, 2012), although IRAP has no canonical NPxY motifs. In 3T3L1 adipocytes, microinjection of the cytoplasmic fraction of IRAP resulted in GLUT4 translocation (Waters *et al.*, 1997), suggesting that IRAP modulates GLUT4 behavior.

In the regulatory mode shift of Tbc1d1, since only temporal Ser-237 phosphorylation with AICAR pretreatment was sufficient for subsequent insulin-induced GLUT4 liberation along with Thr-596 (but not Ser-237) phosphorylation, it is tempting to speculate that the PTB1 domain is responsible for the functionally crucial status of Tbc1d1 without relying on the phosphorylation status of Ser-237 upon executing the regulatory mode shift of Tbc1d1 that might be achieved by associating with unspecified PTB-binding partner(s). Future studies are warranted to determine such interacting molecule(s) for understanding GLUT4 behavior and glucose metabolism. It is also worth noting that the Tbc1d1 subcellular localization detected by conventional immunofluorescence analysis was not apparently changed during exposure to various stimuli (unpublished observations), suggesting further complexity in Tbc1d1 regulation. It is also possible that other phosphorylation sites of Tbc1d1 undergo more prolonged or slow-onset phosphorylation in response to AICAR treatment and are involved in the regulatory mode shift of Tbc1d1 in conjunction with the PTB1 domain. Future detailed investigations of the molecular mechanisms underlying the actions of Tbc1d1 are anticipated to unveil these regulatory complexities.

GLUT4 behavior in cells coexpressing AS160 and Tbc1d1

Unlike adipocytes predominantly expressing AS160, skeletal muscles express both AS160 and Tbc1d1 (Taylor *et al.*, 2008; Castorena *et al.*, 2011). Therefore it is conceivable that GLUT4 behavior in skeletal muscle cells is more complex than that in adipocytes. Previous observations suggested that actions of Tbc1d1 dominate over those of AS160 since ectopic expression of Tbc1d1 strongly inhibited insulin-responsive GLUT4 translocation in 3T3L1 adipocytes (Roach *et al.*, 2007; Chavez *et al.*, 2008). This inhibitory action partially diminished in the presence of AICAR, indicating that Tbc1d1 and AS160 have distinct modes of action in regulating GLUT4 translocation, which is consistent with the present observations. As mentioned before, AS160 also has PTB domains that may modulate in vivo glucose metabolism. Therefore it is possible that AS160 PTB domains also have similar regulatory mechanisms and that the distinct binding properties of 14-3-3 with AS160 and Tbc1d1, in concert with the regulatory mode shift of Tbc1d1, which appear to be dominant over AS160 actions, are key factors determining GLUT4 behavior after various stimuli in skeletal muscle.

Both AS160 and Tbc1d1 have RabGAP activities with nearly similar specificities in vitro (Miinea *et al.*, 2005; Roach *et al.*, 2007). Rab GTPases are major regulators of vesicle transport and have been implicated in multiple steps of vesicle trafficking, including vesicle budding, movement, and tethering/docking and fusion with the plasma membrane (Stenmark, 2009). The human genome encodes >60 members of the Rab family, which are localized to distinct intracellular compartments, and many Rab proteins have been implicated in GLUT4 trafficking (Stockli *et al.*, 2011). Although it is difficult to pinpoint the functions of individual Rab proteins in GLUT4 trafficking, a recent live-cell total internal reflection fluorescence (TIRF) imaging study obtained direct evidence suggesting that different Rab proteins regulate distinct GLUT4-trafficking steps (Chen *et al.*, 2012). Therefore it is possible that different Rab proteins are involved in distinct regulatory modes of Tbc1d1. Although TIRF microscopy is a superior method for analyzing cellular events beneath the plasma membrane, this approach cannot examine the events occurring deeper within the cells. Because our GLUT4 nanometry can easily detect intracellular GLUT4 behavior with high precision,

our approach has the potential to be a powerful tool for unveiling the roles of specific Rab proteins in intracellular trafficking.

In summary, on the basis of our previous and present results, we have clearly demonstrated the similarities and differences between functional roles of two key RabGAPs, AS160 and Tbc1d1, in static GLUT4 liberation, using GLUT4 nanometry and a cell-based reconstitution model, respectively. Based on these lines of evidence, further analysis in cells coexpressing both RabGAPs will provide knowledge promoting better understanding of GLUT4 behavior in skeletal muscle and therefore exercise physiology.

MATERIALS AND METHODS

Plasmids and antibodies

The HaloTag-Tbc1d1 expression vector was from Promega (Madison, WI). The sequence was based on human Tbc1d1. All mutations were generated by PCR-based site-directed mutagenesis and confirmed by sequencing (PRISM 3130; Applied Biosystems, Foster City, CA). Antibodies against phospho-Tbc1d1/S237 and phospho-Tbc1d1/T596 of Tbc1d1 were generated by immunizing rabbits with KLH-conjugated peptides (H-CRPMRKSFpSQPGLRS-OH for phospho-Tbc1d1/S237 or H-CRRANpTLSHFP-OH for phospho-Tbc1d1/T596), followed by immunoaffinity purification using SulfoLink Coupling Gel (Pierce, Rockford, IL). Anti-myc monoclonal antibody (9E10) was purified from hybridoma culture supernatants. Antibodies against pACC, pAkt (Ser473), and Akt were purchased from Cell Signaling (Beverly, MA).

Cell culture

All experiments were performed in 3T3L1 fibroblasts exogenously expressing myc-GLUT4-ECFP, sortilin–enhanced yellow fluorescent protein (EYFP), and/or HaloTag-Tbc1d1. Cells were plated onto glass-bottom dishes (thickness, 0.17 mm; Matsunami Glass, Osaka, Japan) or six-well culture plates and then transfected with Lipofectamine 2000 (Invitrogen, Carlsbad, CA) with plasmid DNA (each 1–2 μg) according to the manufacturer's instructions. For imaging experiments, the cells were immersed in a solution containing 150 mM NaCl, 5 mM KCl, 2 mM $CaCl_2$, 1 mM $MgCl_2$, 10 mM 4-(2-hydroxyethyl)-1-piperazineethanesulfonic acid–NaOH (pH 7.4), and 5.5 mM D-glucose.

Protein detections

Before electrophoresis, cell lysates were incubated with HaloTag TMR Ligand (Bio-Rad, Hercules, CA) for 1 h to fluorescently label HaloTag-fused proteins. Fluorescence of HaloTag TMR Ligand and EYFP were detected with PharosFX Molecular Imager (Bio-Rad) equipped with 488- and 532-nm lasers. Western blotting analyses were performed following standard procedures, and chemiluminescence was detected with ImageQuant LAS4000 mini (GE Healthcare Life Sciences, Piscataway, NJ). Quantification was performed with ImageJ (National Institutes of Health, Bethesda, MD) or ImageQuant TL (GE Healthcare Life Sciences). We calculated the ratio of intensities between phosphorylated and total HaloTag-Tbc1d1, and mean data obtained from three independent assays are shown.

QD labeling of myc-GLUT4-ECFP

QD-conjugated antibody was prepared as follows. First, the Fab fragment of anti-myc antibody was prepared with a Fab Preparation Kit (Pierce). Then the Fab fragment of anti-myc antibody was conjugated with QD655 using a QD antibody conjugation kit (Invitrogen). The final concentration of the QD655-conjugated antibody was determined by optical density at 632 nm according to the manufacturer's instructions. For labeling, the cells were serum starved and incubated in the presence of 1.5–5 nM QD655-conjugated antibodies for 1 h. The cells were then extensively washed to remove unbound QD-labeled antibodies, followed by an additional incubation for at least 3 h.

Single-particle tracking and movement analysis

Imaging experiments were performed with a homemade microscope consisting of an inverted microscope (IX71, Olympus), an electron-multiplying charge-coupled device camera (iXon 887; Andor Technology, Belfast, United Kingdom), a Nipkow disk confocal unit (CSU10; Yokogawa, Tokyo, Japan), and an oil-immersion objective lens (UPLSAPO100xO, numerical aperture 1.4; Olympus, Tokyo, Japan) at ~30°C. QD655 fluorescence was excited at 532 nm with a solid-state laser (Spectra-Physics, Santa Clara, CA) and detected through a 655/12 bandpass filter (Semrock, Rochester, NY). In these experiments, expressions of sortilin-EYFP and HaloTag-Tbc1d1 were confirmed by EYFP fluorescence and by staining of cells with HaloTag Ligand TMR, respectively. Single-particle tracking was performed with G-Count (G-Angstrom, Sendai, Japan) with a two-dimensional Gaussian fitting mode. We tracked each particle successfully fitted within an 8 × 8 pixel region of interest for at least 30 frames. When the signal in a frame was lost because of blinking, no fitting was performed until reappearance of the bright spot. When a bright spot did not reappear within 10 frames, tracking was aborted. We typically tracked 50–150 particles per cell and obtained the images in at least three independent experiments. We evaluated movements with velocity distributions, mean velocities, and diffusion coefficient maps. The velocities for individual particle movements were calculated by linear fit of the displacement during four frames. Mean velocities and frequency distributions were first calculated in a cell and then averaged among cells under the same treatment conditions. We found that QDs in fixed cells showed non-negligible velocities (~0.29 μm/s), believed to be derived from inevitable instrumental noise (Fujita *et al.*, 2010). Thus, in figures representing mean velocities, instead of raw data we used "corrected" values obtained by subtracting the noise. Diffusion coefficients of individual molecules were estimated as follows. First, mean-square displacement (MSD) values of individual particles were calculated with

$$\mathrm{MSD}(n\Delta t)=\frac{1}{N-n}\sum_{i=1}^{N-n}(p_{i+n}-p_i)^2 \qquad (1)$$

where N, n, Δt, and p are the total number of positions measured, the measurement index (going from 1 to $N-1$), the time interval between two consecutive image sequences, and the positions of the molecule, respectively. The diffusion coefficient of the molecule was calculated by fitting the first 10 time points of the MSD values with

$$\mathrm{MSD}(n\Delta t)=4D_{10}n\Delta t+C \qquad (2)$$

where D_{10} and C are the diffusion coefficient of the first 10 time points and instrumental noise, respectively. The MSD and D_{10} calculations and D_{10} map constructions were performed with a custom-written program based on LabVIEW and Vision (National Instruments, Austin, TX).

Photolysis of caged compounds and monitoring of $[Ca^{2+}]_i$

The acetoxymethyl (AM) ester forms of Ca^{2+} indicator fluo-4 (Invitrogen) and caged Ca^{2+} compound NPE (Invitrogen) were first dissolved in dimethyl sulfoxide at 10 mM and then diluted in serum-free DMEM. Cells were incubated for 30 min at 37°C in serum-free DMEM containing 10 μM NPE-AM and 0.03% Cremophor EL

(Sigma-Aldrich, St. Louis, MO) in the presence or absence of 10 μM fluo-4-AM and then washed with imaging buffer. Photolysis of NPE was induced with a mercury lamp (U-ULS100HG, Olympus) through a 360-nm bandpass filter. The mercury lamp radiation was gated with an electric shutter (SSH-R; Sigma Koki, Tokyo, Japan) with an opening duration of 0.1 s. Uncaging experiments were performed under yellow light illumination to prevent unintended photolysis of NPE. Fluo-4 fluorescence was excited at 488 nm with a solid-state laser (Spectra-Physics) and detected through a 530/40 bandpass filter (Olympus). Fluorescence intensities were obtained by ImageJ.

Statistical analyses

Data are represented as mean ± SEM. The Kolmogorov–Smirnov test was used to compare velocity distributions, the Mann–Whitney *U* test or Wilcoxon signed-rank test was used for mean velocities unless otherwise indicated, and $p < 0.05$ was considered to be statistically significant.

ACKNOWLEDGMENTS

We thank Fumie Wagatsuma and Natsumi Emoto for their technical assistance. This study was supported by grants from the Japan Society for the Promotion of Science (22590969 and 20001007). This study was also partially supported by the Banyu Life Science Foundation International and the Takeda Science Foundation. H.H. is a Research Fellow of the Japan Society for the Promotion of Science.

REFERENCES

An D, Toyoda T, Taylor EB, Yu H, Fujii N, Hirshman MF, Goodyear LJ (2010). TBC1D1 regulates insulin- and contraction-induced glucose transport in mouse skeletal muscle. Diabetes 59, 1358–1365.

Castorena CM, Mackrell JG, Bogan JS, Kanzaki M, Cartee GD (2011). Clustering of GLUT4, TUG and RUVBL2 protein levels correlate with myosin heavy chain isoform pattern in skeletal muscles, but AS160 and TBC1D1 levels do not. J Appl Physiol 111, 1106–1117.

Chavez JA, Roach WG, Keller SR, Lane WS, Lienhard GE (2008). Inhibition of GLUT4 translocation by Tbc1d1, a Rab GTPase-activating protein abundant in skeletal muscle, is partially relieved by AMP-activated protein kinase activation. J Biol Chem 283, 9187–9195.

Chen S, Murphy J, Toth R, Campbell DG, Morrice NA, Mackintosh C (2008). Complementary regulation of TBC1D1 and AS160 by growth factors, insulin and AMPK activators. Biochem J 409, 449–459.

Chen S, Wasserman DH, MacKintosh C, Sakamoto K (2011). Mice with AS160/TBC1D4-Thr649Ala knockin mutation are glucose intolerant with reduced insulin sensitivity and altered GLUT4 trafficking. Cell Metab 13, 68–79.

Chen Y *et al.* (2012). Rab10 and myosin-Va mediate insulin-stimulated GLUT4 storage vesicle translocation in adipocytes. J Cell Biol 198, 545–560.

Dash S *et al.* (2009). A truncation mutation in TBC1D4 in a family with acanthosis nigricans and postprandial hyperinsulinemia. Proc Natl Acad Sci USA 106, 9350–9355.

Fujita H, Hatakeyama H, Watanabe TM, Sato M, Higuchi H, Kanzaki M (2010). Identification of three distinct functional sites of insulin-mediated GLUT4 trafficking in adipocytes using quantitative single molecule imaging. Mol Biol Cell 21, 2721–2731.

Goodyear LJ, Kahn BB (1998). Exercise, glucose transport, and insulin sensitivity. Annu Rev Med 49, 235–261.

Hatakeyama H, Kanzaki M (2011). Molecular basis of insulin-responsive GLUT4 trafficking systems revealed by single molecule imaging. Traffic 12, 1805–1820.

Jedrychowski MP, Gartner CA, Gygi SP, Zhou L, Herz J, Kandror KV, Pilch PF (2010). Proteomic analysis of GLUT4 storage vesicles reveals LRP1 to be an important vesicle component and target of insulin signaling. J Biol Chem 285, 104–114.

Kane S, Lienhard GE (2005). Calmodulin binds to the Rab GTPase activating protein required for insulin-stimulated GLUT4 translocation. Biochem Biophys Res Commun 335, 175–180.

Koumanov F, Richardson JD, Murrow BA, Holman GD (2011). AS160 phosphotyrosine-binding domain constructs inhibit insulin-stimulated GLUT4 vesicle fusion with the plasma membrane. J Biol Chem 286, 16574–16582.

Larance M *et al.* (2005). Characterization of the role of the Rab GTPase-activating protein AS160 in insulin-regulated GLUT4 trafficking. J Biol Chem 280, 37803–37813.

Meyre D *et al.* (2008). R125W coding variant in TBC1D1 confers risk for familial obesity and contributes to linkage on chromosome 4p14 in the French population. Hum Mol Genet 17, 1798–1802.

Miinea CP, Sano H, Kane S, Sano E, Fukuda M, Peranen J, Lane WS, Lienhard GE (2005). AS160, the Akt substrate regulating GLUT4 translocation, has a functional Rab GTPase-activating protein domain. Biochem J 391, 87–93.

Nedachi T, Fujita H, Kanzaki M (2008). Contractile C2C12 myotube model for studying exercise-inducible responses in skeletal muscle. Am J Physiol Endocrinol Metab 295, E1191–E1204.

Park S, Kim KY, Kim S, Yu YS (2012). Affinity between TBC1D4 (AS160) phosphotyrosine-binding domain and insulin-regulated aminopeptidase cytoplasmic domain measured by isothermal titration calorimetry. BMB Rep 45, 360–364.

Park SY, Jin W, Woo JR, Shoelson SE (2011). Crystal structures of human TBC1D1 and TBC1D4 (AS160) RabGTPase-activating protein (RabGAP) domains reveal critical elements for GLUT4 translocation. J Biol Chem 286, 18130–18138.

Peck GR, Chavez JA, Roach WG, Budnik BA, Lane WS, Karlsson HK, Zierath JR, Lienhard GE (2009). Insulin-stimulated phosphorylation of the Rab GTPase-activating protein TBC1D1 regulates GLUT4 translocation. J Biol Chem 284, 30016–30023.

Peck GR, Ye S, Pham V, Fernando RN, Macaulay SL, Chai SY, Albiston AL (2006). Interaction of the Akt substrate, AS160, with the glucose transporter 4 vesicle marker protein, insulin-regulated aminopeptidase. Mol Endocrinol 20, 2576–2583.

Pehmoller C, Treebak JT, Birk JB, Chen S, Mackintosh C, Hardie DG, Richter EA, Wojtaszewski JF (2009). Genetic disruption of AMPK signaling abolishes both contraction- and insulin-stimulated TBC1D1 phosphorylation and 14-3-3 binding in mouse skeletal muscle. Am J Physiol Endocrinol Metab 297, E665–E675.

Ramm G, Larance M, Guilhaus M, James DE (2006). A role for 14-3-3 in insulin-stimulated GLUT4 translocation through its interaction with the RabGAP AS160. J Biol Chem 281, 29174–29180.

Roach WG, Chavez JA, Miinea CP, Lienhard GE (2007). Substrate specificity and effect on GLUT4 translocation of the Rab GTPase-activating protein Tbc1d1. Biochem J 403, 353–358.

Sano H, Kane S, Sano E, Miinea CP, Asara JM, Lane WS, Garner CW, Lienhard GE (2003). Insulin-stimulated phosphorylation of a Rab GTPase-activating protein regulates GLUT4 translocation. J Biol Chem 278, 14599–14602.

Stenmark H (2009). Rab GTPases as coordinators of vesicle traffic. Nat Rev Mol Cell Biol 10, 513–525.

Stockli J, Fazakerley DJ, James DE (2011). GLUT4 exocytosis. J Cell Sci 124, 4147–4159.

Stolt PC, Bock HH (2006). Modulation of lipoprotein receptor functions by intracellular adaptor proteins. Cell Signal 18, 1560–1571.

Stone S *et al.* (2006). TBC1D1 is a candidate for a severe obesity gene and evidence for a gene/gene interaction in obesity predisposition. Hum Mol Genet 15, 2709–2720.

Taylor EB *et al.* (2008). Discovery of TBC1D1 as an insulin-, AICAR-, and contraction-stimulated signaling nexus in mouse skeletal muscle. J Biol Chem 283, 9787–9796.

Uhlik MT, Temple B, Bencharit S, Kimple AJ, Siderovski DP, Johnson GL (2005). Structural and evolutionary division of phosphotyrosine binding (PTB) domains. J Mol Biol 345, 1–20.

Vichaiwong K, Purohit S, An D, Toyoda T, Jessen N, Hirshman MF, Goodyear LJ (2010). Contraction regulates site-specific phosphorylation of TBC1D1 in skeletal muscle. Biochem J 431, 311–320.

Waters SB, D'Auria M, Martin SS, Nguyen C, Kozma LM, Luskey KL (1997). The amino terminus of insulin-responsive aminopeptidase causes Glut4 translocation in 3T3-L1 adipocytes. J Biol Chem 272, 23323–23327.

Zhou MM, Ravichandran KS, Olejniczak EF, Petros AM, Meadows RP, Sattler M, Harlan JE, Wade WS, Burakoff SJ, Fesik SW (1995). Structure and ligand recognition of the phosphotyrosine binding domain of Shc. Nature 378, 584–592.

J. Magn. Soc. Jpn., 36, 239-244 (2012) <Paper>

Position sensing system using magnetic ribbon type marker

O. Mori, S. Yabukami, O. Ishii*, H. Kanetaka**, T. Ozawa, and S. Hashi***

Faculty of Engineering, Tohoku Gakuin University, *1-13-1 Chuo, Tagajo 985-8537, Japan*

*Graduate School of science and technology studies, Yamagata University, *3-4-33 Zyounan, Yonezawa, 992-8510, Japan*

**Graduate School of Biomedical Engineering, Tohoku University, *6-6 Aoba, Aramaki, Aoba-ku, Sendai 980-8579, Japan*

***Research Institute of Electrical Communication, Tohoku University, *2-1-1 Katahira, Aoba-ku, Sendai 980-8577, Japan*

A position sensing system of nasogastric tube using a wireless magnetic ribbon type marker has been developed. A Qualityfactor of the marker is 121 which is 13 times higher than conventional LC resonated marker. Position accuracy within 6.4mm was obtained when the marker inside a commercial nasogastic tube was parallel translation to 100mm. The marker inside the tube was roughly tracked in esophagus and in trachea of human model.

Key words: wireless magnetic ribbon type marker, position sensing, nasogastric tube

磁性リボンを用いた位置検出システム

森 修, 薮上 信, 石井 修*, 金高弘恭**, 小澤哲也, 栫修一郎***

東北学院大学工学部, 多賀城市中央一丁目 13-1 (〒985-8537)

*山形大学大学院理工学研究科, 米沢市城南 3 町目 4-33 (〒992-8510)

**東北大学大学院医工学研究科, 仙台市青葉区荒巻字青葉 6-6 (〒980-8579)

***東北大学電気通信研究所, 仙台市青葉区片平 2 丁目 1-1 (〒980-8577)

1. はじめに

モーションキャプチャは, 人間や物体の動きを 3 次元で記録・検出する技術である. 検出方法には光学式, 機械式, 磁気式など古くから様々な手法が開発されてきた. その中で磁気式のモーションキャプチャ [1),2)] は磁界を計測対象とするため、光学的に遮蔽された空間でも適用可能である. しかし従来のものはマーカにバッテリーや引き出し線を必要とし, 例えば生体内部等の使用は制約が大きい. 筆者らはこれまでの研究で, マーカへの引き出し線を持たず外来ノイズの影響を受けにくい LC 共振型の磁気マーカを用いた位置検出システムを提案し, マーカの位置および方向が検出可能であることを示した [3),4),5)].

一方医療現場では, 病気や怪我で食事を取れない患者や寝たきりの患者などに対し, 鼻から咽喉・食道を通して胃に直接栄養剤を送り込む経鼻チューブが多く使用されている. しかし近年経鼻栄養チューブ挿入の際に気管への誤挿入事故や挿入のし過ぎにより胃を傷つける事故が散発している [6)]. 従来これらの対策として, X 線によるチューブ挿入の確認や気泡音による確認がなされているが, これらの方法は放射線被曝や信頼性の問題がある. そこで筆者らは, 生体挿入用チューブ先端に細長ワイヤレスの LC 共振マーカを添付した一軸励磁による簡易なチューブの位置検出システムを試作し、おおまかに食道および気管への挿入を見分けることに成功した [7)]. しかし, チューブに添付させる制約上, マーカの構造が煩雑で性能指数が低いことが課題となっていた. そこで今回筆者らは、磁性リボンの磁歪振動を利用した磁気タグマーカに着目した. 磁性リボンを用いたマーカはコイルとコンデンサを使用する従来のものに比べて構造が単純で安価であり, 性能指数が高いため, より精度の高い位置検出が期待できると考えた. 一方これまでに, 磁気タグの磁歪振動および指向性を用いた位置検出システムが報告されている [8)]. しかしこれは直線移動する車両の 1 次的な位置をおおまかに検出するものであり, 本稿の 3 次元位置および 2 方向角 5 自由度の検出には対応していない.

本稿では磁性リボンの磁気マーカを用いて, 想定される位置でマーカ添付チューブを 100 mm 移動させて相対位置精度を評価した. 次にチューブを人体模型に挿入し, おおまかに食道および気管への挿入を見分けることができたため報告する.

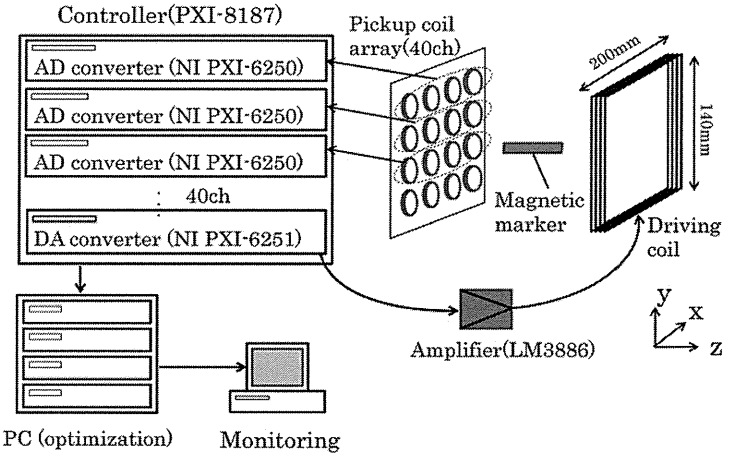

Fig. 1 Schematic diagram of sensing system.

2. 位置計測システムおよび測定方法

Fig. 1は位置検出システムの構成を示したものである．計測システムはマーカ以外は既報[7]と同一の構成であり，励磁コイル，検出コイルアレイ（40チャンネル），磁性リボンマーカ，生体挿入チューブ，ADおよびDAコンバータ（NI PXI-6251：1台），ADコンバータ(NI PXI-6250：10台)，制御ユニット（NI PXI-8187），アンプ（LM3886）から構成される．制御用プログラムはLab VIEW ver. 7.1，最適化処理プログラムはVisual C++を用いて作成した．本システムではマーカ共振周波数の磁界を印加し，磁性リボンの機械的振動による誘導磁界を検出コイルアレイを用いて計測する．AD コンバータのサンプリングは 250 ksample/sec で測定し，マーカの有無における 40ch の検出コイルの誘起電圧の差分からマーカ寄与電圧を求めた．マーカの中心位置および方向はマーカから発生する誘導磁界がダイポール磁界に近似できることを仮定して，(1)～(3)式より Gauss-Newton 法により最適化処理する．

$$S(\vec{p})=\sum_{i=0}^{n}(B_m^{(i)}-B_c^{(i)}(\vec{p}))^2 \tag{1}$$

$$\vec{B}_c^{(i)}(\vec{p})=\frac{1}{4\pi\mu_0}\left\{-\frac{\vec{M}}{r_i^3}+\frac{3(\vec{M}\cdot\vec{r}_i)\cdot\vec{r}_i}{r_i^5}\right\} \tag{2}$$

$$\vec{p}=(x,y,z,\theta,\phi,M) \tag{3}$$

ただし S は評価値であり，$\vec{p}$ はパラメータベクトルである．iは検出コイルの番号（1～40），$\vec{B}_c^{(i)}(\vec{p})$ は双極子磁界を考慮した磁束密度の理論値，$\vec{r}$ はマーカから検出コイル i への位置ベクトル，$\vec{M}$ はマーカ中心の磁気モーメント，(x,y,z) はマーカ iの座標，θは xy 平面へ射影したモーメントの方向ベクトルと x 軸のなす角，φ はモーメントの方向ベクトルと z 軸のなす角である．

Fig. 2(a) は今回使用したマーカの写真である．マーカには防犯 IC タグ(高千穂交易社製 DR ラベル)を加工して使用した．このタグには磁性リボン 2 枚と永久磁石が内蔵されている．Fig. 2(b)はマーカ長手方向の断面図で，内部は磁性リボンと永久磁石の 2 重構造になっている．永久磁石は磁性リボンの長手方向にバイアス磁界を印加している．Fig. 2(c)はカッターを用いてマーカを Table 1 のように小型に加工し，生体用チューブ（富士システムズ製 マーゲンゾンデ S，E-10，外径 6mm，内径 4mm）先端に添付したものである．

3. マーカの評価および実験配置

3-1 マーカの共振特性

Fig. 3 に磁性リボンを用いた共振マーカの動作原理について示す．磁性リボンは幅方向に磁気異方性が付与されている．これに励磁コイルから交流磁界を印加すると，磁気モーメントが若干長手方向に傾く．磁性リボンは磁歪により長手方向に機械的に振動し，誘導磁界が発生する．そして

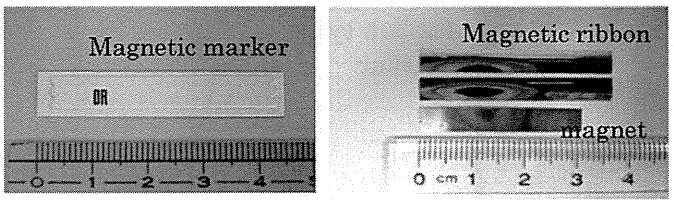

(a) tag

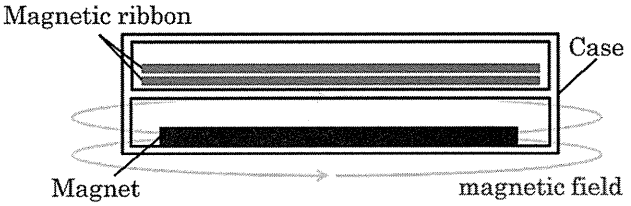

(b) construction of the magnetic ribbon type marker

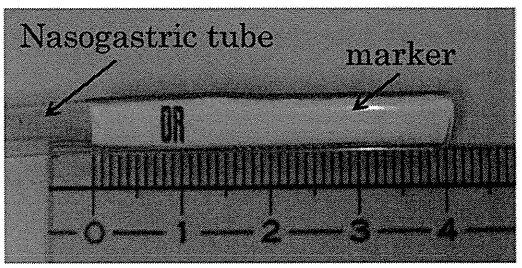

(c) marker in the nasogastric tube

Fig. 2 Magnetic ribbon type marker.

Table 1 Size of magnetic ribbon type marker.

unit:mm

	Before fabrication	Fabricated
Total	45×10×1.9	39×3.8×1.9
Magnetic ribbon	38×5.0×0.03	38×3.6×0.03
Magnet	30×5.0×0.045	30×3.6×0.045

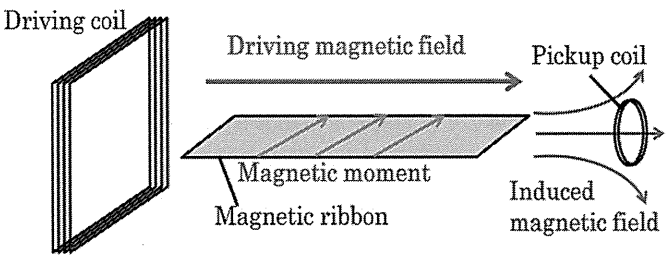

Fig. 3 Principle of operation.

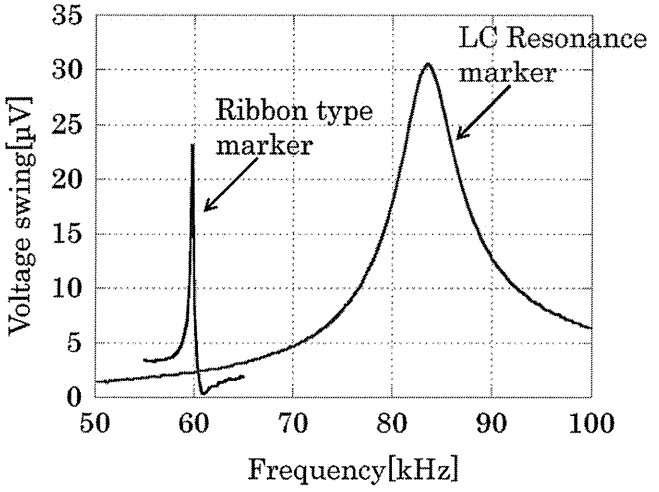

Fig. 4 Comparison of resonance amplitudes.

検出コイルで交流磁界および誘導磁界を測定する．Fig. 4 は既報の LC 共振マーカ [7]及び磁性リボンマーカの共振周波数における誘導電圧のマーカ寄与分を比較したものである．磁性リボンの機械振動を利用した磁気マーカは、電気的に接続している LC 共振回路に比べて振幅が鋭い．それぞれの共振周波数および性能指数は、LC 共振マーカが 83.5 kHz で 9.03，磁性リボンマーカが 59.75 kHz で 121.4 であり，性能指数は約 13.4 倍の値となった．LC 共振マーカは磁性リボンマーカに比べて検出コイルに近い位置で測定を行っているため信号が強い．なお性能指数 Q は (4)式より求めた．

$$Q = \frac{f_r}{\Delta f} \tag{4}$$

ただし f_r は Fig. 4 における共振周波数，Δf は共振周波数におけるマーカ寄与電圧の半値幅である．既報 [3]で述べたように，本マーカの共振時の性能指数が高いことはマーカの損失が小さく，外部へ発生する誘導磁界が大きいことを意味する．この誘導磁界（等価的な磁気モーメント）はマーカを等価的な共振回路とおくと，マーカの性能指数とマーカの断面積の積に比例する [3]．このことから，高い性能指数を有する機械的振動を利用したマーカにより位置検出システムの SN 比が向上すると考えられる．また，本マーカは LC 共振型のマーカに比べて周波数選択性が優れているため，共振周波数の異なる複数のマーカの運用に期待できる．

3-2 マーカの指向性

マーカに対してどの角度から磁界を印加すると効率的に誘導磁界が発生し，正確な位置検出が可能であるか検討した．Fig. 5 は実験配置及びマーカに印加する磁界の方向を示したものである．検出コイルアレイから 300 mm の距離に励磁コイルを対向させるように配置し，その間にマーカを設置した．励磁コイルは 140mm×200mm の長方

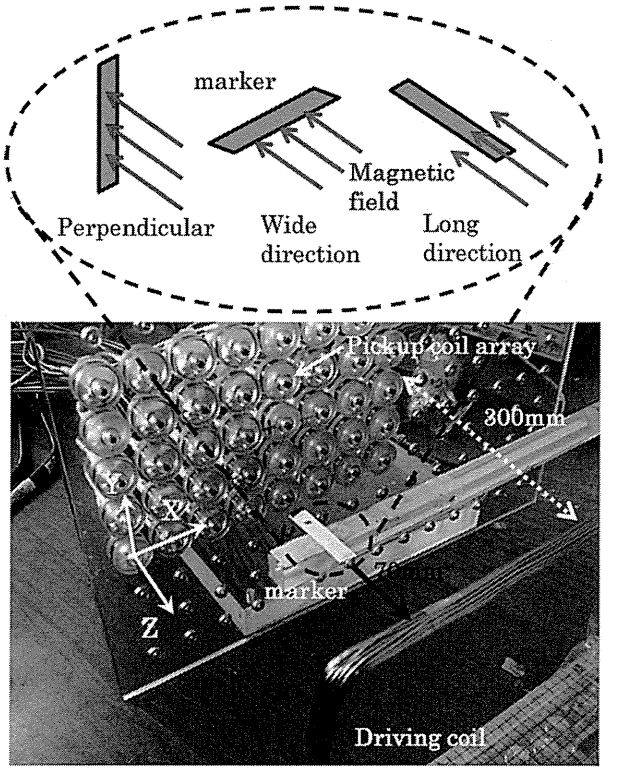

Fig. 5 Examination of directivity.

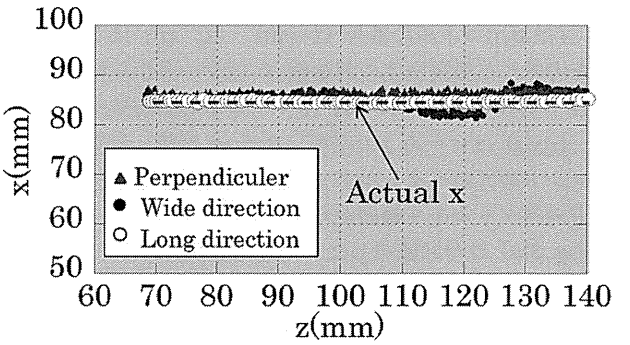

(a) Z-X plane

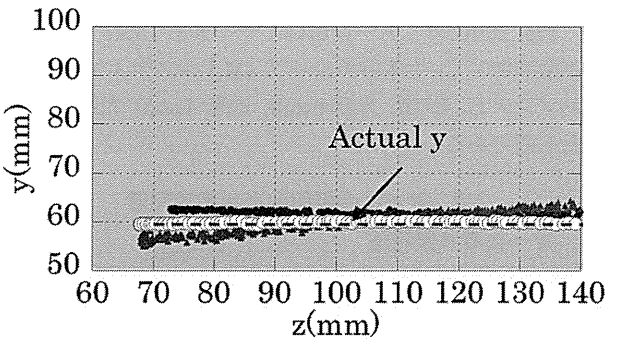

(b) Z-Y plane

Fig. 6 Position tracking in directivity examination.

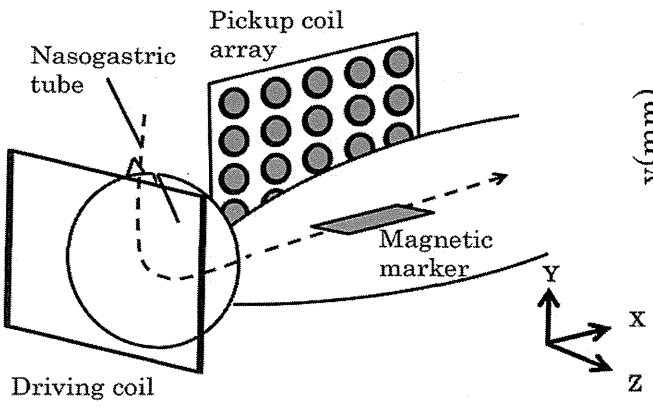

Fig. 7 Experiment arrangement.

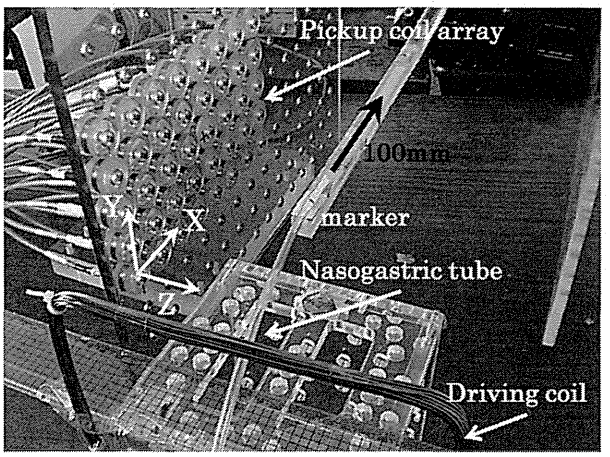

Fig. 8 Position tracking of marker in tube.

形であり，直径 1.0mm の銅線を 30 ターン施した．検出コイルは直径 0.2mm の銅線を直径 23mm，125 ターン施し，同一平面上に 30mm の間隔で 40 個(横:8 個×縦:5 個)配置した．Fig. 5 に示すようにマーカへの印加磁界はそれぞれ面方向，幅方向，長手方向に平行な成分とした．マーカはマイクロメータを用いて，初期値(85,60,70)の位置から z 方向に+70 mm 直線移動させた．Fig. 6 は 3 通りの位置検出の測定結果であり，(a) は Z-X 平面，(b) は Z-Y 平面への射影を示している．▲●○はそれぞれ印加磁界を厚み方向，幅方向，長手方向とした場合の最適化されたマーカの中心位置であり，破線は実際の移動の軌跡である．測定結果を見ると，長手方向に磁界を印加した場合が最も実際の軌跡に追従した．一方主としてマーカの幅方向および厚み方向へ励磁した場合，ある程度マーカ位置は最適化できたものの，精度は悪化した．これは主としてマーカの幅方向や厚み方向に磁界を印加した場合，一部の励磁磁界が長手方向成分を持ち，長手方向に機械的振動を起こしたためと考えられる．しかしこの場合は長手方向へ励磁した場合に比較して機械的振動は小さく，誘導磁界が低減したと考えられる．このことから，マーカの長手方向に磁界を印加するのが適切であると考えられる．

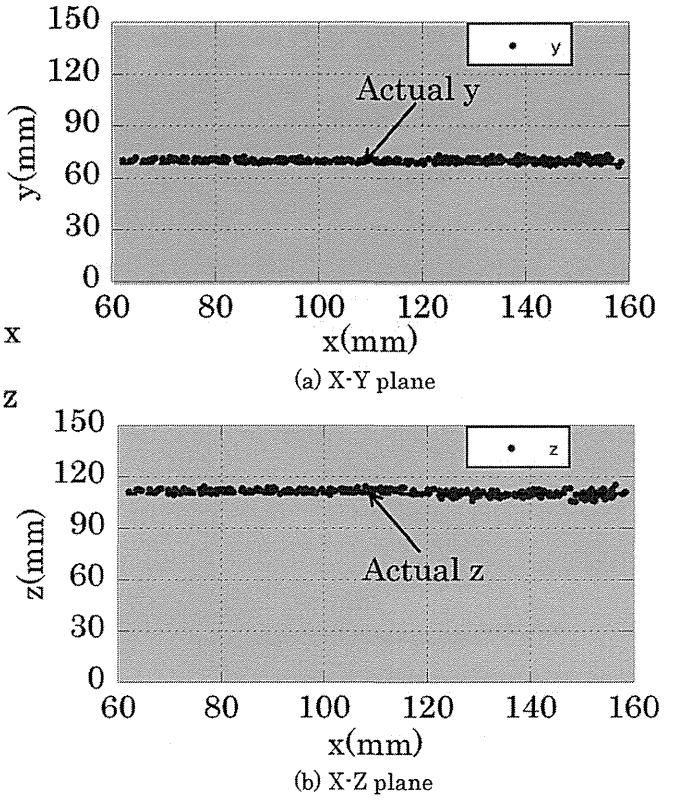

Fig. 9 Positional detection measurement result.

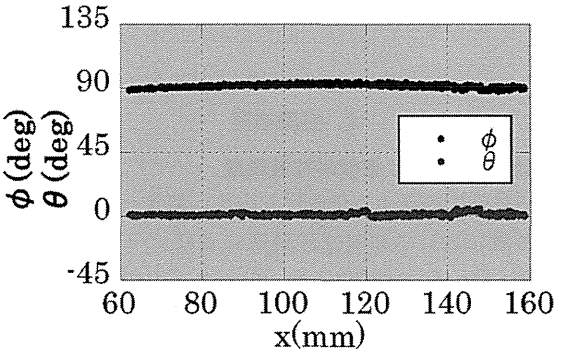

Fig. 10 Direction of marker.

3-3 実験配置

Fig. 7 は想定している励磁コイル，検出コイルおよび磁気マーカの配置を示したものである．マーカをチューブ内部に貼付する際，チューブは円筒型であるためチューブとマーカの長手方向を平行にする必要がある．また，Fig. 7 の指向性の検討より励磁磁界とマーカ長手方向を平行にすることでマーカを効率よく励磁できる．この 2 つの制約から，励磁コイルを人体の頭上に設置し，励磁方向を人体の長手方向と平行にした．一方，検出コイルはマーカからなるべく強い誘導磁界を得るため，マーカに接近させる必要がある．そのため，人体の胸部付近に設置した．励磁コイルと検出コイルのなす角度は約 90° となっている．

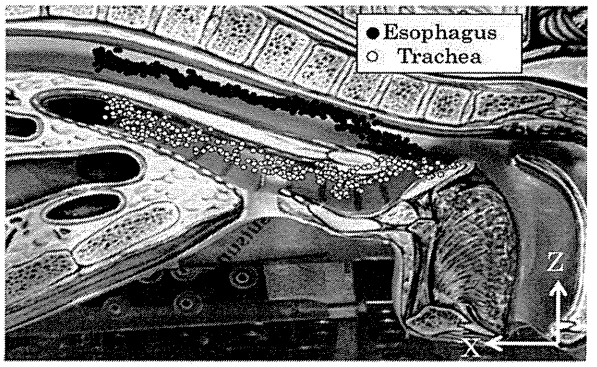

(a) X-Z plane

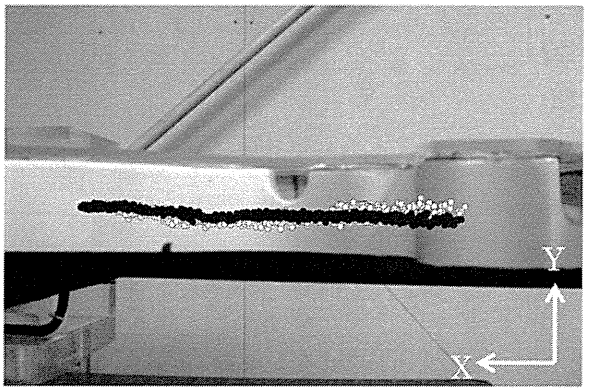

(b) X-Y plane

Fig. 11 Position of the marker in the human model.

4. 実測結果

4-1 直線移動における相対位置精度

食道や気管に相当する位置において，想定する 100mm 程度の移動における相対位置精度およびマーカの向きを評価した．Fig. 8 は励磁コイル，検出コイルの配置およびマーカを移動している写真である．マーカを貼付した生体用チューブ先端をマイクロメータ (SIGMA KOKI 製 LST-16100) およびアクリル棒により検出コイル面から約 110mm の距離 において Fig. 8 の x 方向に+100mm 平行移動した．

Fig. 9 は直線移動時のマーカ中心の軌跡の位置検出結果を示したものである．測定は，マーカを連続的に動かしつつ 10Hz で電圧測定および位置方向を最適化して表示した．(a) は X-Y 平面，(b) は X-Z 平面への射影を示している．●はシステムから得られた測定位置であり，破線は実際の移動の軌跡である．検出された軌跡はほぼ実際の移動距離および軌跡に追従した．100mm 移動での相対位置精度は約 6.4mm 以内であった．Fig. 10 は直線移動時のマーカの向きを φ および θ で検出した結果である．配置したマーカの角度は終始 φ が 90°，θ が 0° であり，実験結果からもこれとほぼ同等の角度が得られた．誤差要因としてはマーカから誘起される磁界とダイポール磁界との誤差，検出コイルのサイズ効果 (測定点が広がりをもつことに起因する誤差)，AD コンバータのノイズレベル等が考えられる．この値はチューブ先端が食道あるいは気管に入ったことを見分ける観点ではほぼ満足すると考えられる．

4-2 人体模型内部での位置精度

Fig. 11 はマーカを貼付した生体用チューブの先端を人体模型の咽頭付近から気管あるいは食道にそれぞれ挿入し，約 100mm 移動させた場合のマーカの中心位置の軌跡を人体模型の写真と重ねて比較したものである．(a) は X-Z 平面，(b) は X-Y 平面への射影を示している．気管内ストロークの初期配置は (35,70,110)，最終配置は (135,70,105) であり，食道内ストロークの初期配置は (35,70,110)，最終配置は (135,70,125) である．食道・気管共に実際の曲線の軌跡にほぼ追従した結果が得られており，チューブ先端位置が気管にあるか食道にあるかの判別が可能と考えられる．

5. まとめ

1. 磁性リボンの機械的振動を用いた磁気マーカによる位置検出システムを開発した．
2. 試作したマーカは 59.75kHz で性能指数は 121.4 であり，既報 [7]のマーカに対して約 13 倍以上の高い値を得た．
3. チューブ添付マーカを x 軸方向に 100mm 平行移動させた場合、相対位置精度は 6.4mm 以内であった．
4. 先端にマーカを貼付した生体挿入用チューブを人体模型に挿入した場合、チューブ先端位置が気管か食道かの判別が可能である。

謝辞 CPI テクノロジーズの高野卓雄氏，高野卓大氏には本システムの制御プログラムの作成におきまして助力を頂きましたことを深く感謝致します．治具製作にご協力頂いた東北学院大学工学部機械工場スタッフの皆様に感謝致します．本研究の一部は科学技術振興機構研究成果最適展開支援プログラム探索タイプの援助を受けた．

Reference

1) J. E. Mcfee, Y. Das, *IEEE Trans. Antennas and Propagation,* vol. **AP-29**, pp. 282-287 (1981).
2) http://www.kbk.co.jp/cesd/polhemus.htm
3) S. Yabukami, S. Hashi, Y. Tokunaga, T. Kohno, K. I. Arai, and Y. Okazaki, *Journal of the Magnetics Society of Japan,* vol. **28**, pp. 877-885 (2004).
4) S. Yabukami, T. Katoh, S. Hashi, K. I. Arai, and Y. Okazaki, *Journal of the Magnetics Society of Japan,* vol. **30**, pp. 218-224, (2006).
5) S. Yabukami, K. Ogasawara, H. Saitoh, S. Hashi, M.

Toyoda, Y. Okazaki, and K. I. Arai, *Journal of the Magnetics Society of Japan*, No. **6**, pp. 439-444, (2007).
6) http://www.med-safe.jp/pdf/report_6.pdf.
7) R. Sato, S. Yabukami, T. Ozawa, H. Kanetaka, S. Hashi, *Journal of the Magnetics Society of Japan*,35(2), 67-71, (2011).
8) W. Suenaga, *Journal of the Magnetics Society of Japan,* **25,** 21 (2001).

2011年11月04日受理, 2012年1月18日採録